

1

Wavelet-based optical flow

2

for two-component wind field estimation

3

from single aerosol lidar data

4

Pierre Dérian, Christopher F. Mauzey and Shane D. Mayor*

5

California State University Chico, Chico, California

6 *Corresponding author address: California State University Chico, 400 W. First St., Chico, CA

7 95928

8 E-mail: sdmayor@csuchico.edu

ABSTRACT

9 A motion estimation algorithm is applied to image sequences produced by
10 a horizontally-scanning elastic backscatter lidar. The algorithm, a wavelet-
11 based optical flow estimator named *Typhoon*, produces dense two-component
12 vector flow fields that correspond to the apparent motion of microscale aerosol
13 features. To validate the efficacy of this approach for the remote measure-
14 ment of wind fields in the lower atmosphere, an experiment was conducted
15 in Chico, California, in 2013 and 2014. The flow fields, estimated every
16 17 s, were compared with measurements from an independent Doppler li-
17 dar. Time-series of wind speed and direction, statistical assessment of the
18 10-min averages and examples of wind fields are presented. The comparison
19 of 10-min averages at 100 m AGL reveals excellent correlations between esti-
20 mates from the *Typhoon* algorithm and measurements from the Doppler lidar.
21 Power spectra and spectral transfer functions are computed to characterize the
22 filtering effects of the algorithm in the spatial domain.

23 **1. Introduction**

24 Motion estimation is a branch in the field of computer vision that develops algorithms to deter-
25 mine the apparent movement of objects in sequences of digital images. Since the seminal paper
26 by Horn and Schunck (1981), the applications of these numerical methods have become numer-
27 ous; they play key roles in the success of many modern technologies including bioinformatics,
28 video compression and machine vision. These techniques are also commonly found in experimen-
29 tal fluid dynamics, applied for example to particle image velocimetry (PIV) (Adrian 2005). In
30 contrast to in-situ measurements which are inherently restricted to a single point of space, motion
31 estimation methods are non-intrusive and provide fields or volumes of velocity vectors and thus
32 offer a broader perspective of the flow.

33 Because of the abundance of images in the atmospheric and oceanic sciences, motion estimation
34 has been practiced since before the digital age. For example, determination of the movement of
35 cloud or water vapor features in satellite images was done prior to the work of Horn and Schunck
36 (1981) through a block-matching approach (Leese et al. 1971). These atmospheric motion vectors
37 (AMV) constitute nowadays an essential component of the observations assimilated by numerical
38 weather prediction models (García-Pereda and Borde 2014). Other modern applications involve
39 for example the recovery of glacier velocities (Scambos et al. 1992), displacements resulting from
40 landslides (Stumpf et al. 2013), surface water flows (Dugan et al. 2014) and breaking waves dy-
41 namics (Melville and Matusov 2002).

42 Another application, similar to PIV and AMV, involves the estimation of 2D, 2-component wind
43 field from the apparent motion in aerosol backscatter lidar data (Schols and Eloranta 1992). Thus
44 far the motion estimation algorithms used in that context were variations of the cross-correlation
45 method (Mayor et al. 2012; Hamada et al. 2015). In this paper, a more recent approach that

46 was devised specifically for application to fluid motion is investigated. This algorithm, named
47 *Typhoon*, is a wavelet-based optical flow estimator. It was previously validated with synthetic and
48 real PIV images (Dérian 2012). Here, as a first step, the validity of this wavelet-based optical flow
49 approach in the context of atmospheric lidar data is demonstrated.

50 The paper is organized as follows: Section 2 introduces the motion estimation framework for the
51 wind measurement problem and the traditional cross-correlation algorithm. Section 3 presents the
52 proposed *Typhoon* algorithm. The input aerosol backscatter lidar data is detailed in Section 4. Fi-
53 nally, in Section 5, estimated wind fields are validated by comparisons with remote measurements
54 from a commercial Doppler lidar. Power spectra and transfer functions are calculated to show the
55 filtering effect of the proposed approach.

56 **2. Wind measurement and motion estimation**

57 *a. Wind measurement strategies*

58 Air motion is represented by a three-component vector and may be defined at all points in the
59 atmosphere. The wind is generally regarded as the vector consisting of two horizontal components.
60 Active remote wind measurement techniques may be subdivided into Doppler and non-Doppler
61 approaches.

62 Ground-based radars and lidars typically collect data in a spherical coordinate system. Doppler
63 radars and lidars directly measure only the radial (line-of-sight) component of air motion. For a
64 Doppler radar or lidar to measure the wind, specific scanning strategies and assumptions about the
65 air motion over space and time must be made. Wind profiling describes the use of a remote sensor
66 to provide a vertical profile of horizontal wind vectors at a single location above the surface of the
67 earth. Alternatively, two Doppler radars or lidars, separated by some horizontal distance, may be

68 used to probe an area from different angles and obtain a two-component wind field. This approach
69 is known as “dual-Doppler” (Stawiarski et al. 2013).

70 Non-Doppler approaches estimate wind fields from the spatial and temporal movement of fea-
71 tures observed by the instrument. Eloranta et al. (1975) provided some of the first remote wind
72 measurements by lidar in the lower atmosphere. Since that time, hardware and software has ad-
73 vanced greatly and a small number of validation experiments have been conducted, e.g. Mayor
74 et al. (2012). Meanwhile, other fields, in particular experimental fluid dynamics, have developed
75 similar approaches to retrieve motions. This concept is also known to the computer vision com-
76 munity, where it is associated with the wide family of *motion estimation* techniques.

77 *b. Fluid motion estimation: the vision approach*

78 The idea of using the *apparent motion of tracers* to infer the invisible underlying fluid flow is
79 not new. It “could probably be traced far back in history to the first time a person possessing
80 the concept of velocity watched small debris moving on the surface of a flowing stream” (Adrian
81 2005). Many visualization methods have been developed, such as using droplets, dye, smoke or
82 shadows for the purpose of revealing fluid flow structures and dynamics (Van Dyke 1982). This
83 led in particular to the well-known PIV techniques, which have been used in experimental fluid
84 dynamics for almost 30 years (Adrian 2005). Our 2D, 2-component wind measurement approach
85 fits in the motion estimation context: the tracers are the aerosol *features*, visualized by the lidar
86 system, and the motion estimation technique is usually the cross-correlation. This configuration
87 is very comparable to PIV, with the important differences that the distribution of aerosols in the
88 atmosphere (the “seeding” of the flow) cannot be controlled, and that the images are not of indi-
89 vidual particles, but instead of a field that approximately represents particle concentration (Held
90 et al. 2012). In these aspects, this problem is closer to AMV computation. An important difference

91 is the temporal and spatial resolutions covered by these two approaches: typically, on the order of
 92 15 seconds and 10 meters for the considered lidar data, versus 15 minutes and several kilometers
 93 for geostationary satellite imagery (García-Pereda and Borde 2014).

94 *c. Motion estimation framework*

95 Motion estimation aims to recover the apparent displacements within a sequence of images.
 96 The time and space variations of an observable image quantity are used to infer the underlying
 97 motion field occurring in the image plane between two consecutive frames of the sequence. In this
 98 work, input images are the scans provided by the lidar, the movements of the variations of aerosol
 99 backscatter intensity are used to estimate the wind field.

100 In the following, the scan domain is noted as $\Omega \subset \mathbb{R}^2$. The observable backscatter intensity is
 101 noted as $I_n(\mathbf{x})$ at pixel $\mathbf{x} = (x_1, x_2) \in \Omega$ and at discrete time $t_n, n \in \mathbb{N}$. The *apparent displacement*
 102 between two consecutive scans I_n, I_{n+1} is a 2D vector field \mathbf{u} :

$$\mathbf{u}(\mathbf{x}, t_n) = \begin{pmatrix} u_1(\mathbf{x}, t_n) \\ u_2(\mathbf{x}, t_n) \end{pmatrix}.$$

103 This displacement is measured in pixel units and occurs over the time $\delta t_n = t_{n+1} - t_n$ s. If the scan
 104 has a resolution of δx m pixel⁻¹, an estimation of the *instantaneous wind velocity* \mathbf{v} in m s⁻¹ is
 105 therefore given by:

$$\mathbf{v}(\mathbf{x}, t_n) = \frac{\delta x}{\delta t_n} \mathbf{u}(\mathbf{x}, t_n). \quad (1)$$

106 As such, the motion is assumed to be stationary during the time step δt .

107 Velocity components v_1, v_2 are the *in-plane* components, that is, they belong to the image plane.
 108 Due to the very low value of the elevation angle of the lidar scan plane (typically $< 6^\circ$), these
 109 components coincide with the horizontal wind components (usually denoted u, v in atmospheric

110 sciences). The *out-of plane* component (normal to the scan plane), which remains unestimated,
111 thus corresponds to the vertical component w .

112 The question of the accuracy of motion estimation techniques is often raised. The answer is
113 complex, since it involves the *data characteristics* (spatial, temporal resolutions), the information
114 given by the *visualization method* (the image content), and the underlying *motion field* itself. In
115 the current context, the later contributions are difficult to quantify, as they depend largely on the
116 conditions (e.g., the presence of particulate matter, the scales and variability of the wind field).
117 However, assuming ideal conditions and a perfect model, errors related to the resolution of data
118 may be quantified. If displacements are measured as integers on the image grid, the systematic
119 error is ± 0.5 pixel, which then gives $\pm 0.5\delta_x/\delta_t$ m s⁻¹ for each motion component. In practice,
120 various interpolation techniques allow for sub-pixel estimation, reducing this error. The error can
121 be also lowered by using a smaller δ_x and/or a larger δ_t . However, for a given motion field, a
122 smaller δ_x results in larger apparent displacements, which can be more challenging for estima-
123 tion algorithms. On the opposite, larger δ_t leads to less accurate perception of the instantaneous
124 velocity, since the assumption of stationarity of the motion field is less valid over longer periods.

125 Any motion estimation technique features two main aspects. The first one, known as the *data*
126 *model*, describes the link between observations I (the aerosol backscatter intensity) and the under-
127 lying unknown displacement \mathbf{u} . This model should take into account the nature of observed data
128 and its relevant dynamics. Then, as an inverse problem, motion estimation is usually ill-posed.
129 The second aspect is therefore the *regularization*, which is required in order to close the estima-
130 tion problem. The regularization may also provides information where the data model fails locally.
131 The various estimation techniques feature different data models, regularizations or implementation
132 strategies.

133 *d. The cross-correlation algorithm, concept and limitations*

134 The cross-correlation technique performs independent, local motion estimations on subregions
 135 (blocks) of the scan domain. It consists in correlating a block of the first scan I_n with a translated
 136 block of the second scan I_{n+1} ; the translation vector \mathbf{u} which induces a correlation peak is consid-
 137 ered to be the displacement at the center of the block (Schols and Eloranta 1992). The estimation
 138 problem, presented in its basic form, is written as:

$$\forall \mathbf{x} \in \Omega_C, \mathbf{u}(\mathbf{x}, t_n) = \arg \max_{\mathbf{u}} \sum_{\mathbf{y} \in B(\mathbf{x})} \frac{[I_{n+1}(\mathbf{y} + \mathbf{u}) - \mu_{n+1}(\mathbf{x} + \mathbf{u})][I_n(\mathbf{y}) - \mu_n(\mathbf{x})]}{\sigma_{n+1}^2(\mathbf{x} + \mathbf{u})\sigma_n^2(\mathbf{x})}, \quad (2)$$

139 where $\Omega_C \subset \Omega$ is the set of block centers (and therefore the set of locations of estimated vectors),
 140 $B(\mathbf{x})$ is the block centered on \mathbf{x} , $\mu_p(\mathbf{x})$ and $\sigma_p(\mathbf{x})$ are the mean and standard deviation, respectively,
 141 of backscatter intensity I_p over block $B(\mathbf{x})$. Note that in practice, this cross-correlation function
 142 (CCF) is computed using the FFT for computational efficiency.

143 In this case, the data model is the CCF (2) itself; the regularization is implicitly given by the
 144 size of block $B(\mathbf{x})$ which should be large enough to contain reliable information, yet as small as
 145 possible to resolve small scale motions. Typically, neighboring blocks overlap by 50%, so that the
 146 estimated motion field is *sparse* (fewer motion vectors than pixels). Each vector is the result of
 147 a single *independent* problem, which makes the CCF algorithm pleasingly parallel (Mauzey et al.
 148 2012). This cross-correlation approach and its numerous variants have become widely used in PIV
 149 (Adrian and Westerweel 2010); in geosciences it is often applied to satellite imagery to retrieve for
 150 instance glacier velocities (Scambos et al. 1992). It is also the standard method to derive AMVs
 151 (Schmetz et al. 1993; García-Pereda and Borde 2014), and has given good results with aerosol
 152 backscatter lidar data, as shown in Schols and Eloranta (1992), Mayor and Eloranta (2001) and
 153 Mayor et al. (2012).

154 However, this method as presented in (2) is not exempt from drawbacks. First, the displace-
155 ment within an entire block $B(\mathbf{x})$ is explained by a single vector $\mathbf{u}(\mathbf{x})$, which implies that this
156 displacement is assumed to be uniform (constant) over the block. The larger the block, the less
157 likely this assumption is to be true. Yet, as overly small blocks may result in uncertainties due to
158 lack of information, “large” blocks are usually preferred. This leads to the second point: as dis-
159 placements occurring within large blocks are likely not uniform, the estimated $\mathbf{u}(\mathbf{x})$ corresponds
160 to a power-weighted average of the apparent displacements within the corresponding block $B(\mathbf{x})$
161 (Hamada 2014), which results in an over-smoothed motion field. To address these issues, this
162 study proposes to evaluate a recently developed motion estimation algorithm dedicated to fluid
163 flows.

164 **3. Typhoon algorithm**

165 Early attempts with a different class of motion estimation methods, often called *optical flow*,
166 were conducted in 2010 on the CHATS¹ dataset and led to promising results (Dérian et al. 2010).
167 Since then the authors developed a new version of the algorithm based on a *wavelet* framework,
168 named *Typhoon*. The extensive description of the algorithm is largely mathematical and details
169 regarding the design of the data-model and the regularization can be found in Dérian et al. (2013)
170 and Kadri Harouna et al. (2013), respectively. In the following, an overview of the method and the
171 improvements made to achieve real-time wind estimation from aerosol backscatter lidar imagery
172 are provided.

¹Canopy Horizontal Array Turbulence Study, near Dixon, CA, 2007 – see Patton et al. (2011).

173 *a. Optical flow, from observations to motion*

174 The proposed approach has two major differences with respect to the cross-correlation algorithm
 175 presented above. First, this wavelet-based optical flow uses a *global* formulation: all vectors $\mathbf{u}(\mathbf{x})$
 176 of the displacement field \mathbf{u} are estimated simultaneously by solving a single problem, whereas
 177 the cross-correlation approach in (2) has as many independent problems as vectors $\mathbf{u}(\mathbf{x})$. Second,
 178 this method provides a *dense* estimate, that is to say one displacement vector at every point \mathbf{x}
 179 of the scan domain Ω , whereas the CCF solution is usually sparse. The estimate is obtained by
 180 minimizing a functional, similar to an energy, defined over the whole scan domain:

$$\mathbf{u} = \arg \min_{\mathbf{u}} \left\{ \frac{1}{2} \int_{\Omega} [f_{data}(I, \mathbf{u})]^2 d\mathbf{x} + \frac{\alpha}{2} \int_{\Omega} [f_{reg}(\mathbf{u})]^2 d\mathbf{x} \right\}. \quad (3)$$

181 f_{data} is the data model that depends on observations I and unknown displacement \mathbf{u} , while the
 182 regularization f_{reg} depends on \mathbf{u} only. The parameter $\alpha > 0$ balances the two terms and is fixed by
 183 the user.

184 The data model used in *Typhoon* is known as the displaced frame difference (DFD):

$$I_{n+1}(\mathbf{x} + \mathbf{u}(\mathbf{x}, t_n)) = I_n(\mathbf{x}). \quad (4)$$

185 It is analogous to finding the displacement field \mathbf{u} that “warps” an image into the next one. This
 186 model assumes the *consistency of backscatter intensity* along the trajectory of an aerosol feature
 187 during the time interval $[t_n; t_{n+1}]$, that is to say an aerosol feature will present the same intensity,
 188 the same “signature”, in both scans I_n, I_{n+1} . Therefore any phenomena inducing a significant
 189 change in intensity, such as turbulent diffusion or out-of-plane motion, can possibly lead to *false*
 190 *apparent motions*.² Such phenomena are not uncommon, but it can be reasonably assumed that
 191 the time scales at which they act are significantly larger than the inter-scan time-step δt_n , so that

²False apparent motions refer here to illusory motions of aerosol features that do not correspond to the horizontal wind.

192 the DFD (4) remains valid. It is also important to note that from formulation (3), the data model is
193 not *strictly* enforced. Instead, the solution achieves a balance between trying to follow the model
194 on one hand and the regularization on the other – hence the role of the parameter α , which allows
195 the user to give more weight to one term over the other.

196 Regularization schemes usually encourage the estimate \mathbf{u} to follow some *smoothness assumption*
197 *tion*. This work uses the most simple first-order regularization, originally introduced in Horn and
198 Schunck (1981), which penalizes strong velocity gradients. For each displacement component u_i ,
199 $i = 1, 2$:

$$f_{reg}(u_i) = |\nabla u_i| = \sqrt{\left(\frac{\partial u_i}{\partial x_1}\right)^2 + \left(\frac{\partial u_i}{\partial x_2}\right)^2}. \quad (5)$$

200 Note that the square root is later cancelled by the square in (3). If the regularization is given much
201 more weight than the data model ($\alpha \rightarrow \infty$ in (3)), the solution that minimizes (3) moves toward
202 a uniform motion field (with $\nabla u_i = 0$ for $i = 1, 2$). The regularizer also takes precedence over
203 the data model locally where the latter is inefficient, for instance within uniform regions of the
204 input images. Other regularizers are available in *Typhoon*, penalizing, for instance, the vorticity or
205 divergence of the flow, or the gradient of vorticity, divergence; some of these schemes have proven
206 to be very efficient with PIV and water vapor satellite images (Corpetti et al. 2002). However, as
207 the regularization becomes more complex, the associated computational costs increase, which may
208 reduce the ability to achieve real-time estimation. Moreover, in the context of aerosol backscatter
209 lidar images, little to no improvement brought by the use of these advanced schemes was found.
210 This could be linked to the specificities of this lidar data, which will be detailed further in Section 4.

211 The DFD model (4) and the Horn and Schunck regularizer (5) inserted into (3) complete the
 212 motion estimation problem:

$$\mathbf{u}(t_n) = \arg \min_{\mathbf{u}} \left\{ \frac{1}{2} \int_{\Omega} [I_{n+1}(\mathbf{x} + \mathbf{u}(\mathbf{x}, t_n)) - I_n(\mathbf{x})]^2 d\mathbf{x} \right. \\ \left. + \frac{\alpha}{2} \int_{\Omega} \sum_{i=1,2} |\nabla u_i(\mathbf{x}, t_n)|^2 d\mathbf{x} \right\}. \quad (6)$$

213 A particularity of this problem is that the DFD model (4) is not linear in \mathbf{u} , so that the whole func-
 214 tional is not quadratic. This complicates the minimization process, as the existence of a global
 215 minimum is not guaranteed. This is another role for the regularization term: it convexifies the
 216 functional as $\alpha \rightarrow \infty$. But, as large α values are unmanageable, to ensure a successful mini-
 217 mization it is important for the solution \mathbf{u} to lie “close” to the first guess.³ This calls for the use
 218 of an incremental strategy, often known as “*multi-resolution*”: the displacement field is estimated
 219 following a coarse-to-fine process, starting with coarse structures of large amplitudes, and progres-
 220 sively refining toward smaller scales. This last point motivates the use of the *wavelet framework*.

221 *b. Introduction to the wavelet framework*

222 In signal processing, the spectral space is often used to analyze or exhibit some properties of a
 223 given signal. The FFT leads to a representation in terms of sine and cosine functions of specific
 224 frequencies. Any spatial information is lost in the process: the Fourier coefficients, which form
 225 an equivalent representation of the input signal, yield no information as to *where* their associated
 226 frequency is or is not present. This is due to the fact that the sine and cosine functions, which form
 227 the basis of the spectral space, are very well localized in frequency but have an infinite support in
 228 space. Conversely, looking at the signal in the physical space does not give any information on the
 229 frequency content. The wavelet formalism offers a trade-off: the wavelet functions are localized
 230 both in space and frequency, thus they enable access to information on the *frequency content and*

³which is usually the null motion field, $\mathbf{u}(\mathbf{x}) = 0 \forall \mathbf{x} \in \Omega$.

231 *the spatial location* simultaneously – at the cost of lower precision. A wavelet representation of
232 a given signal consists of a *coarse approximation* of the signal, along with several sets of *details*
233 containing spatially-localized information at various ranges of frequencies. Note that instead of
234 frequency, the wavelet formalism prefers the equivalent but reciprocal notion of *scale*.

235 This multi-scale (or, multi-resolution) representation offered by the wavelet transform is the
236 main motivation to adopt wavelet bases for displacement components u_1, u_2 . It leads to a “natu-
237 ral” coarse-to-fine strategy suitable to motion estimation (Dérian et al. 2013). Approximation and
238 coarse detail coefficients are estimated first, then fine-scale details are successively added until the
239 smallest scale is reached. Besides the multi-scale framework, wavelet bases also allow the rep-
240 resentation of arbitrary regular functions (a 3D fluid motion field should at least be continuous).
241 While the continuity might not be a relevant assumption for the 2D field, a sufficient regularity is
242 required in order to compute the regularizing terms presented in Section 3.a, which involve spa-
243 tial derivatives. Finally, these regularization schemes find a relatively simple yet very accurate
244 implementation in that context (Kadri Harouna et al. 2013). Similarly to the Fourier transform,
245 the wavelet transform is a linear, separable⁴ operator, with fast algorithms (fast wavelet transform,
246 FWT) for computational efficiency. Wavelets are also used in many fields, from signal denois-
247 ing to video compression; Mallat (2008) discusses an extensive presentation of the theory and
248 applications.

249 Conceptually, the use of wavelet bases does not lead to significant changes to the estimation
250 problem (6). Each motion component u_i is expressed as the inverse transform (reconstruction) of
251 its corresponding wavelet coefficients c_i :

$$u_i = W_{inv}(c_i), \quad i = 1, 2,$$

⁴The 2D transform is obtained by combining two 1D transform, first along rows then along columns.

252 where W_{inv} denotes the inverse wavelet transform. The set of wavelet coefficients $\{c_1, c_2\}$ thus is
253 the unknown to the estimation problem.

254 *c. Recent improvements*

255 The original algorithm detailed in Dérian et al. (2013) would accept square images only. If
256 input images were rectangular, they had to be padded to turn them square, which increases the
257 computational burden. The current version has been modified to accept rectangular images.

258 The main improvement is the result of redesigning the code to run in “real-time”. To keep up
259 with real-time, the estimate of wind field $\mathbf{v}(t_n)$ from scans I_n, I_{n+1} must be complete by the time
260 the next scan I_{n+2} is made available, with the inter-scan time-step δt_n typically on the order of
261 10 to 20 seconds. Since the whole motion field is estimated simultaneously, the number of vari-
262 ables is quite large: a dense estimate from 512×512 pixel images represents about half a million
263 unknowns. Wavelet transforms lie at the core of the estimation process. Each evaluation of the
264 functional (6) requires two inverse FWTs (to reconstruct the displacement \mathbf{u} from its coefficients)
265 and two forward FWTs (to compute the gradient). In order to achieve the necessary reduction in
266 computation time, the low-level functions of the algorithm – in particular, the wavelet transforms
267 – were rewritten in *CUDA language*, which enables it to execute on NVIDIA’s graphic processing
268 units (GPU). GPUs designed for scientific computing rely on several thousands of small com-
269 puting units, thus providing massive parallelization capabilities. The CUDA version of *Typhoon*
270 running on an NVIDIA GeForce GTX Titan is 10 to 100 times faster than the original version
271 (Mauzey et al. 2014), and is sufficient to meet the real-time requirements.

272 4. Application to aerosol backscatter data

273 The results presented hereafter have been obtained from data collected by the Raman-shifted
274 Eye-safe Aerosol Lidar (REAL) (Mayor and Spuler 2004; Spuler and Mayor 2005; Mayor et al.
275 2007; Spuler and Mayor 2005) in 2013 and 2014 in Chico, California. The REAL is a ground-
276 based, scanning, elastic backscatter lidar operating at a wavelength of 1.54 microns, with a pulse
277 energy typically between 120 and 170 mJ, a pulse rate of 10 Hz and a pulse duration of 6 ns. It
278 employs 40 cm diameter optics and an analog direct detection receiver. The backscatter signal is
279 sufficiently strong from a single pulse that averaging over multiple pulses is not required. This
280 section describes the input scan data as well as the preprocessing steps.

281 *a. Data preprocessing*

282 Before motion estimation takes place, the raw signal delivered by the REAL must be prepro-
283 cessed. Lidar data is sampled on a polar grid, with the lidar at the origin. Each scan is composed
284 of *shots*, with a shot being a 1D array of backscatter samples, uniformly spaced along the range r
285 every 1.5 m, collected at a given angular position θ from a single laser pulse.

286 The raw backscatter intensity $I_{raw}(r, \theta)$, with the range r and the azimuth angle θ , corresponds
287 to the actual backscatter signal $\beta(r, \theta)$ and an additive noise $\varepsilon(r, \theta)$.

$$I_{raw}(r, \theta) = \beta(r, \theta) + \varepsilon(r, \theta).$$

288 The noise ε combines contributions from the atmosphere and the instrument and can be modeled
289 by a random variable which follows a normal distribution of mean μ_θ and standard deviation σ_θ .
290 Values of μ_θ , σ_θ change slightly from one shot to another, hence their dependency in θ ; they can
291 be estimated for each shot from background data. As explained in Mayor et al. (2012), first the

292 noise mean is subtracted:

$$I_0(r, \theta) = I_{raw}(r, \theta) - \mu_\theta = \beta(r, \theta) + \varepsilon_0(r, \theta),$$

293 with $\varepsilon_0(r, \theta) = \varepsilon(r, \theta) - \mu_\theta$ the now centered random noise. The raw signal-to-noise ratio (SNR)
294 is computed at that point:

$$SNR_{raw}(r, \theta) = \frac{I_0(r, \theta)}{\sigma_\theta}. \quad (7)$$

295 Shots are then multiplied by the square of the range to compensate for the one-over-range-squared
296 decay of the backscatter β :

$$I_{r^2}(r, \theta) = r^2 I_0(r, \theta) = r^2 \beta(r, \theta) + r^2 \varepsilon_0(\theta).$$

297 Note that the noise amplitude now increases as the square of the range. For optimal results, it is
298 then essential to discard irrelevant noisy data, which is discussed further.

299 After conversion to decibels, shots are filtered in the range dimension. The low-pass median
300 filter of length 7 points (10.5 m) removes high-intensity spikes typically caused by hard-targets
301 such as birds and insects, while the high-pass median filter of length 333 points (500 m) removes
302 the very large structures to reveal local fluctuations. Figure 1 presents an example of preprocessed
303 backscatter data (panel a), along with the corresponding raw SNR (7) (panel b).

304 *b. Detecting coherent features*

305 Two different aspects complicate the motion estimation process. First, due to the nature of
306 backscatter data, the raw SNR (7) decays as one-over-range-squared. Typically, for the REAL
307 operating in Chico, CA, the SNR resulting from a single laser pulse drops below 5 at $r = 3$ km.
308 Such high levels of noise in the far range are challenging for optical flow. Second, for the purpose
309 of motion estimation, a good SNR in the near range does not necessarily imply useful information.

310 For instance, coherent features can be absent from a region of the scan, yielding much uncertainties
 311 as to the underlying wind field in that region.

312 In order to maximize the quality of the results, the scan areas presenting no coherent aerosol fea-
 313 tures are discarded. Because of the regularization schemes provided by optical flow (Section 3.a),
 314 wind vectors estimated over noisy areas *could* be relevant. However judging so proves to be diffi-
 315 cult, as often even a basic visual confirmation is impossible in noisy regions. Hence, it is safer to
 316 simply discard the noisy image data before motion estimation.

317 To detect the presence of coherent aerosol features, the *image SNR* is used. It is defined as the
 318 ratio of the *local* standard deviation of coherent signal $\sigma_\beta(r, \theta)$ to the *local* standard deviation of
 319 noise σ_ε :

$$SNR_{img}(r, \theta) = \frac{\sigma_\beta(r, \theta)}{\sigma_\varepsilon(r, \theta)}. \quad (8)$$

320 This ratio is estimated from the autocovariance function of preprocessed data $I(r, \theta)$. For every
 321 point (r, θ) , the autocovariance C_l is computed along the range from data in $[r - l/2; r + l/2]$.
 322 Then, the local variance of coherent signal is given by the average of coefficients at lag 1 and -1:

$$(\sigma_\beta)^2 = 0.5(C_l(-1) + C_l(1)),$$

323 while the local variance of noise is obtained from the 0-lag coefficient and σ_β :

$$(\sigma_\varepsilon)^2 = C_l(0) - (\sigma_\beta)^2.$$

324 An example of image SNR is shown in Fig. 1 panel c. A 256-point window was used to compute
 325 the autocovariance, corresponding to $l = 384$ m.

326 From the image SNR, a valid data domain is computed for each scan. It is assumed that the best
 327 data is in the near range, therefore the valid domain is simply defined by a far-range boundary. For
 328 each shot (azimuth θ), this far-range boundary is given by the smallest range $R(\theta)$ above which

329 the image SNR remains below a threshold τ fixed by the user:

$$\forall \theta, R(\theta) = \min_R \{R : \forall r > R, SNR_{img}(r, \theta) < \tau\}. \quad (9)$$

330 Finally, a low-pass median filter of width 25 points and a Gaussian filter of parameter $\sigma = 2$
331 points are applied to the set of $R(\theta)$, to exclude small isolated features and smooth the boundary.
332 An example of mask representing the valid data domain is shown in Fig. 1 panel d, using $\tau = 3$.

333 *c. Correction of image distortions*

334 A lidar scan does not correspond to an instantaneous view of the aerosol distribution. The shots
335 that compose the scan are acquired sequentially. In the event of high wind speeds, this leads to
336 apparent distortions of the aerosol features in the lidar images, which in turn causes the estimated
337 motion to be biased. This issue was first noted by Sasano et al. (1982) who proposed an iterative
338 correction method. Assuming that the aerosol features are transported *without deformation* by a
339 uniform wind vector, scans can be warped to reconstruct an approximated instantaneous view of
340 the aerosols, thus improving the accuracy of motion estimation. In this study, implementation
341 proceeds as follows for a given scan pair:

- 342 i. Estimate the displacement field \mathbf{u} from the pair of scans with the *Typhoon* algorithm.
- 343 ii. Convert to velocity field \mathbf{v} using (1).
- 344 iii. Correct both scans for distortions using wind field \mathbf{v} , following Sasano et al. (1982). The time
345 of the beam at the center of the scan is used as the reference time.
- 346 iv. Repeat i–iii until mean wind speed $|\bar{\mathbf{v}}|$ changes by either less than 1%, or less than $0.25\delta_x/\delta t$.
347 Typically, it requires 2-3 iterations.

348 The correction step (iii) is carried on the polar grid data. After correction, backscatter data is no
349 longer known on a regular polar grid, but instead is at scattered locations.

350 *d. Cartesian gridding*

351 After preprocessing, masking and correction for distortions, the backscatter data is interpolated
352 on a Cartesian grid of spacing $\delta x = 8$ m. It is possible to perform the motion estimation directly
353 on the original polar grid, however, as mentioned above, the correction step destroys the regularity
354 of the mesh. Fast interpolation on large sets of scattered data can be challenging, considering
355 real-time requirements. In this work, a CUDA implementation of nearest-neighbor interpolation
356 was used.

357 **5. Validation**

358 A field experiment was conducted in Chico, CA, from mid-September 2013 to mid-January
359 2014, to validate the wind fields recovered by *Typhoon*. A Doppler lidar (DL) was deployed to
360 provide independent wind measurements. It is a pulsed, heterodyne detection Doppler lidar com-
361 mercialized by HALO Photonics under the name Stream Line (Pearson et al. 2009). This model
362 was previously certified against cup anemometer measurements (Axel and Ailt-Wiard 2014), and
363 showed very good agreement to radar wind profiler and radiosonde (Päschke et al. 2014). The DL
364 has the S/N 0811-35 and was built in November 2011. It operates at a wavelength of 1.5 microns,
365 pulse energy of $20 \mu\text{J}$, pulse rate of 15 kHz, and a pulse duration of 150 ns. DL data was fil-
366 tered following the manufacturer’s indications, keeping only points for which the minimum SNR
367 intensity > 1.01 .

368 Since it is not possible to retrieve a 2D 2-component wind field using a single DL, two different
369 configurations were investigated.

- 370 • *Temporal validation.* The DL was located at 1500 m range, 15° azimuth from the REAL
371 and operated in vertical profiling mode. Data from this configuration enable comparisons of

372 time-series of 2-component wind velocities at the DL location. This phase of the experiment
373 was conducted during September and October 2013.

- 374 • *Spatial validation.* The DL was located on the roof of the REAL container and operated
375 in fixed-beam mode, staring at the center of the sector scan area swept by the REAL. This
376 configuration enables one to compare *radial wind* velocity components along the DL line-of-
377 sight. Data for this second phase of the experiment were collected in December 2013 and
378 January 2014.

379 The main parameters used by both systems during these two experiments are summarized in Ta-
380 ble 1.

381 a. *Temporal validation*

382 In this experiment, the REAL scans between -15° and 45° azimuth, with a 4° elevation, every
383 17 s. This places the scan at 100 m AGL at the range of the DL. The DL operates in vertical
384 profiling mode (VAD scan), providing a profile of 2-component horizontal wind vector about
385 every 15 s.

386 A typical example of aerosol motion estimation is presented in Fig. 2. It features a close-up of
387 two motion fields estimated from three successive position plan indicator (PPI) scans. The flow is
388 relatively uniform, and can be visually identified due to a large aerosol feature that moves toward
389 the southeast. The DL wind vectors at 100 m AGL are displayed for comparison and show a good
390 agreement with the *Typhoon* estimates.

391 In this paper, an effort is made to establish the potential of the *Typhoon* algorithm when applied
392 to aerosol backscatter lidar data. However, quality of the data depends upon the performance of
393 the instrument and the state of the atmosphere. Therefore, we selected the days presenting the

394 best potential for this validation among data collected in Chico, CA from mid-September to mid-
395 November 2013, with the expectation that future advances in hardware will lead to increases in
396 data quality and availability. First, due to the local typical conditions in Chico, aerosol backscatter
397 imagery is much better for this application during the daytime than during nighttime. There-
398 fore, this study was restricted to daytime only. Second, the percentage of valid backscatter data
399 (Sec. 4.b), during daytime, in a 50 m radius around the DL were computed. These values are
400 plotted against the mean wind speed measured by the DL the same day in Fig. 3. With a suffi-
401 cient spatial distribution of aerosol features, dense 2-component wind fields can be delivered up to
402 several km in range. Figure 4 shows an example of such wind field on a day with high speed and
403 uniform direction, with vectors available out to 4 km range. The low-SNR area in the far-range
404 were dynamically excluded. Figure 5 presents a view of a ≈ 200 m vortex, illustrating the ability
405 of *Typhoon* to extract coherent structures at intermediate scales.

406 Three specific cases are described below: light, moderate and strong wind conditions. These
407 days are represented by solid diamonds in Fig. 3. For each case, time-series of instantaneous and
408 10-min averaged wind measurements are presented. 10-min averages are the reference measures
409 for instrument validation in the wind power industry (Bailey 2012). Then, statistics on 10-min
410 averages for the 15 days having more than 85% valid data are presented.

411 The VAD scan strategy used by the DL assumes that the wind is uniform throughout the swept
412 area (Mann et al. 2009, 2010; Sathe et al. 2011; Sathe and Mann 2012); in this case this region is a
413 disc of about 100 m radius, represented by a turquoise circle in Figs. 4 and 5. In order to compare
414 results of the study to the DL measures, instantaneous *Typhoon* estimates are averaged in space
415 over a similar sized area centered on the DL location.

416 Occasionally, the estimation may fail and result in obvious outliers. Those outliers can be de-
417 tected and removed under the assumption of temporal coherence of the wind field. The *normalized*

418 *median test*, commonly used in PIV (Adrian and Westerweel 2010), was implemented. Similar
419 concepts are used with radar wind profilers (Weber et al. 1993). Within each 10-min window, the
420 median wind vector \mathbf{v}_m is computed, as well as the residuals $r(\mathbf{v}) = |\mathbf{v}_m - \mathbf{v}|$ for each vector \mathbf{v} of
421 the window. Vectors for which the residual $r(\mathbf{v})$ is twice larger than the median of residuals r_m are
422 discarded.

423 1) LIGHT WIND CASE

424 Figure 6 shows wind speed and direction measured by the DL at 100 m AGL and estimated
425 by *Typhoon* for a 12-hour period starting on October 23 at 15:00 UTC. It is a light wind episode
426 with speeds remaining below 3 m s^{-1} and variable direction. Estimates are missing over a pe-
427 riod approximatively covering 15:00 to 17:00 UTC. This is due to the coherent feature detection
428 presented in Sec. 4.b: no significant features were present in the region of interest at that time,
429 therefore no motion estimates are available. Then, between 17:00 and 18:00 UTC, *Typhoon* speed
430 and direction estimates are in systematic error. Visual inspection of the aerosol imagery reveals
431 the mixed layer growing with the entrainment zone passing through the altitude of the intercom-
432 parison. It appears that the plumes and wind shear in the entrainment zone result in false apparent
433 motions that bias the motion estimations. Later, two reversals of wind direction occurred at 22:30
434 and 23:30 UTC that correspond to the passage of a vortex of diameter $\approx 200 \text{ m}$ over the region
435 of interest (see also Fig. 5 for a spatial visualization). This microscale circulation resembles those
436 that have resulted from large eddy simulation of convective boundary layers (Schmidt and Schu-
437 mann 1989; Kanak 2005; Sullivan and Patton 2011). Correlation coefficients R^2 for the 10-min
438 averaged wind components are 0.951 and 0.600 for u and v , respectively. Excluding the 17:00 –
439 18:00 UTC period with false apparent motions, R^2 values increase to 0.966 and 0.866.

440 2) MODERATE WIND CASE

441 Figure 7 shows wind speed and direction measured by the DL at 100 m AGL and estimated
442 by *Typhoon* for a 12-hour period starting on September 17 at 15:00 UTC. This wind episode fea-
443 tures speeds ranging 0 to 10 m s⁻¹ and direction mostly stationary except for a 2-hour fluctuating
444 episode (corresponding to the lowest wind speeds). Wind speed is underestimated at two occa-
445 sions, both corresponding to rapid and large changes in direction around 22:30 and 23:00 UTC.
446 Otherwise, both series of data are in very good agreement. This is confirmed by the 10-min aver-
447 aged wind components: correlation coefficients R^2 are 0.979 and 0.991 for u and v , respectively.

448 3) STRONG WIND CASE

449 Figure 8 shows wind speed and direction measured by the DL at 100 m AGL and estimated
450 by *Typhoon* for a 12-hour period starting on October 9 at 15:00 UTC. It is a strong wind episode
451 with speeds up to 16 m s⁻¹ and very consistent flow from the northwest direction. Both time-
452 series are again in very good agreement. Correlation coefficients R^2 for the 10-min averaged wind
453 components are 0.984 and 0.929 for u and v , respectively.

454 4) OVERALL CONSIDERATIONS

455 Scatter plots of 10-min averaged wind components measured during the daytime⁵ for the 15
456 “best” days (Fig. 3) are presented in Fig. 9. They show an overall excellent agreement of *Typhoon*
457 estimates with DL measurements at 100 m AGL: correlation coefficients R^2 are 0.995 and 0.997
458 for u and v , respectively. Detailed statistics on u and v are available in Tables 2 and 3. In terms of
459 wind speed, a linear regression gives a slope of 1.000 with an offset of -0.10 m s⁻¹, R^2 coefficient

⁵“Daytime” is arbitrarily considered to be 15:00 – 01:00 UTC (10 hours).

460 is 0.991. Regarding the wind direction, the offset is 1.1° and R^2 coefficient is 0.944.⁶ This $\approx 1^\circ$
461 offset observed for the direction corresponds to the precision at which the DL was oriented during
462 its deployment. The root mean square error (RMSE) between *Typhoon*'s estimates and the DL
463 observations is 0.29 m s^{-1} on both on u and v components. This is slightly higher than the expected
464 systematic error of $0.5\delta_x/\delta_t \approx 0.24 \text{ m s}^{-1}$ which assumes perfect data and model (Sec. 2.c). The
465 few remaining outliers mostly correspond to false apparent motions, typically occurring at the
466 beginning and end of the day as the boundary layer depth evolves.

467 From the time-series shown in Figs. 6, 7 and 8, it appears the variability of the wind speed
468 obtained by *Typhoon* is less than that measured by the Doppler. Figure 10 is a scatter plot of
469 turbulent kinetic energy (TKE) as measured by the Doppler and *Typhoon* over 10-min intervals.
470 A linear regression suggests that the TKE from *Typhoon* is about 50% smaller than the Doppler's.
471 This could be linked to the fact that *Typhoon* measures apparent displacements, which are later
472 converted to velocities (Sec. 2.c). Small-scales velocity structures, either in time or space, are
473 less accurately perceived. Using a faster scan rate is likely to improve the results. Nevertheless,
474 *Typhoon* performs better than the cross-correlation technique: the optimized algorithm presented
475 in Hamada et al. (2015) recovers 39% of the TKE on the same dataset.

476 *b. Spatial validation*

477 During this phase of the experiment, the DL was colocated with the REAL. The REAL swept
478 between 15° and 75° azimuth at 2° elevation every 17 s. The DL held its beam fixed at 45° azimuth
479 and 2° elevation, measuring the radial velocity component as a function of range and time. DL
480 measurements were integrated over one second, with a range gate of 48 m. The temporal resolution

⁶When dealing with circular data such as angles, the slope for the linear regression should be fixed to 1. The offset and R^2 only are computed, see e.g. Fisher (1995).

481 of DL measurements is therefore much finer than that of the REAL flow fields, and conversely for
482 the spatial resolution (see Table 1).

483 Instead of holding the DL beam fixed, a PPI sweeping strategy identical to the REAL's could
484 have been used, thus allowing the comparison of radial components over the whole scan domain.

485 However, two arguments support the choice of a fixed beam:

- 486 • With a moving beam set-up, the integration time for DL measurements was reduced to less
487 than 0.1 s. This would cause the SNR to decrease very rapidly. Typically in Chico the
488 maximum range with useful data would be on the order of 1500 m, significantly below that
489 of the REAL's.
- 490 • The radial velocity fields collected by the DL would suffer from the same distortions as the
491 backscatter data (Section 4.c), so correcting these distortions would be challenging.

492 The data used for the spatial validation were recorded in December 2013 and January 2014. In
493 Chico, CA, the days are shorter and the air is cleaner during this season than in the autumn when
494 time-series data were collected. Both the DL and the REAL are affected. Data are of lower quality
495 than shown for the temporal validation. The availability of 10-min averages falls below 50% after
496 3 km for both instruments and at 5 km it is below 5%. Therefore, the analysis is restricted to the
497 first 3 km. Furthermore, it should be noted that the prevailing wind direction during this time over
498 Chico, CA is northwesterly. At 45° azimuth, the line-of-sight component corresponds mostly to
499 the *cross-stream*, turbulent wind perturbations. In these data, its magnitude remains mostly below
500 3 m s⁻¹. Figure 12 shows a comparison of radial velocity measured by the DL and extracted from
501 the 2-component fields obtained by *Typhoon* for a 8-hour period starting 8 January 2014 at 17:00
502 UTC.

503 In order to compute statistics, radial velocities were averaged. First, spatial resolution are
504 matched by averaging *Typhoon* velocities in space according to DL range gates, then 10-min time-
505 averages are computed at every range. A scatter plot of these 10-min averages is presented in
506 Fig. 13, along with linear regression slopes, R^2 coefficient and distribution of differences. These
507 values were obtained from 8-hour periods (17:00 to 01:00 UTC) for 8 days of December 2013 and
508 January 2014. The R^2 coefficient (panel d) decreases with the range and this is expected as both
509 instruments are affected by the gradual reduction in SNR. R^2 remains above 0.95 over the first
510 1.5 km, then slowly decreases to about 0.8 at 3 km. The overall R^2 is 0.928. While the relation
511 between *Typhoon* and DL velocities remains linear, the slope (panel c) increases with the range,
512 from about 0.95 at 0.5 km to 1.3 at 3 km. Velocities obtained by the cross-correlation method
513 show a similar trend (Hamada et al. 2015). This leads to a theory that these discrepancies are due
514 to a mismatch in the actual elevation angles of the beams during this phase of the experiment,
515 especially considering the unbiased results of the temporal validation. At a lower elevation angle
516 and therefore lower altitude, the DL would measure lower velocities.

517 *c. Spectral analysis*

518 In this section, temporal and spatial power spectra of the velocity components produced by
519 *Typhoon* are presented, with the objective of characterizing the filtering effect of the algorithm –
520 in particular, in the spatial domain. The velocity data analyzed were collected during the daytime
521 and within the turbulent lower atmospheric boundary layer.⁷ Therefore, an inertial subrange in the
522 power spectra of the actual velocity field is expected.

⁷RHI scans collected every 15 min by the REAL during the 15 days included in the analysis show that the maximum convective boundary layer height, that typically occurred in the afternoon, ranged from 300–1200 m AGL.

523 The spectra are computed in natural coordinates to account for the anisotropy of atmospheric
524 boundary layer turbulence. The west-east and south-north wind velocity components are projected,
525 according to the mean wind direction, as streamwise (u_s) and cross-stream (v_n) components, such
526 that u_s carries the mean speed and v_n has a null mean. The mean wind vector is defined accordingly
527 to the investigated dimension, either in time or space. The spectra are finally averaged together
528 according to the mean wind speed, using bins of 0–4 m s⁻¹, 4–8 m s⁻¹, 8–12 m s⁻¹ and 12–
529 16 m s⁻¹, in order to exhibit their evolution with increasing wind speed and turbulent kinetic energy.
530 The resulting power spectral densities (S) are multiplied by frequency (f) or wavenumber squared
531 (κ^2) so that an inertial subrange would appear as a $-2/3$ slope and white noise would appear as
532 $+1$ slope.

533 1) TEMPORAL POWER SPECTRA

534 During the experiment, the REAL collected PPI scans every 17 s and one RHI scan every 15 min.
535 The RHI scan resulted in an 30 s interruption of the PPI scan sequence. The scan strategy of the
536 DL provided vertical profiles of horizontal winds every 15 ± 1 s. Since the FFT requires data
537 points at a uniform time interval, the *Typhoon* and DL wind measurements were interpolated to
538 a 5 s time series. From the 5 s time series data, we computed power spectra over consecutive
539 10 min intervals. The 10-min mean wind vector was used for the projection in natural coordinates
540 and the binning of spectra, as defined above. The resulting spectra have a Nyquist frequency of
541 0.029 Hz (34 s period) for the *Typhoon* velocities and 0.033 Hz (30 s period) for the DL. The
542 lowest frequency is 1.67×10^{-3} Hz (10 min period).

543 The spectra are presented in Fig. 14. Those from the Doppler lidar are consistently higher than
544 the spectra from *Typhoon*, this is consistent with our observation that the TKE measured from
545 Doppler velocities are larger than those from *Typhoon* (Fig. 10). The temporal spectra appear to

546 become flatter as the mean wind speed increases. We hypothesize that this may be caused by the
547 challenges that both *Typhoon* and the DL face under windy conditions. For the DL, increased
548 variability of the actual wind velocity field in the VAD sample area results in more error in the
549 horizontal wind vector estimate. The increased error appear as noise at these time scales and
550 flatten the spectrum. For *Typhoon*, windy conditions result in larger horizontal displacements
551 between scans and faster deformation of aerosol coherent structures.

552 2) SPATIAL POWER SPECTRA

553 An independent observation of the 2-component 2-D velocity field does not exist for comparison
554 with those produced by *Typhoon*. A dual-Doppler lidar set up could have provided it, but would
555 have doubled the cost and complexity of the project. Therefore, to investigate the integrity of the
556 vector flow fields in space, spatial power spectra are considered.

557 A 1 km diameter circular area is considered, centered on the DL at 1.53 km range. All of the
558 vectors within this area (from a single flow field in time) are used to compute the spatial mean wind
559 vector, which then define a natural coordinate system. Vectors of the flow field are interpolated on
560 a 128×128 point grid ($1024 \text{ m} \times 1024 \text{ m}$) that is centered on the DL and aligned with the natural
561 coordinate system, and then projected as streamwise (u_s) and cross-stream (v_n) components. This
562 operation was performed for each flow field independently and resulted in 30092 flows fields over
563 15 days. At 4° elevation, the $1024 \text{ m} \times 1024 \text{ m}$ area covers a range of altitudes from about 50 m
564 to 150 m AGL. A possible impact of this is that the turbulence statistics within this sloped domain
565 are slightly inhomogeneous. Nevertheless, for each component u_s , v_n , the 2D power spectral
566 densities computed by FFT for each flow field are averaged together according to the mean spatial
567 wind speed. Finally, slices of the resulting 2D power spectra were extracted along the streamwise
568 and cross-stream directions. This results in four 1D spectra for each wind speed bin: along the

569 streamwise and cross-stream directions, for each of the streamwise and cross-stream components.
570 The Nyquist wavenumber is $\kappa/2\pi = 0.0625 \text{ m}^{-1}$ (16 m wavelength), the lowest wavenumber is
571 $9.77 \times 10^{-4} \text{ m}^{-1}$ (1204 m).

572 The spectra in the top row of Fig. 15 show the TKE increasing as expected as function of wind
573 speed. Each spectrum has a maximum amplitude at low wavenumbers. We hypothesize that the
574 peak corresponds to one over the Eulerian length scale, and is within the energy containing range
575 (Kaimal and Finnigan 1994). However, the spectra are steeper than $\kappa^{-2/3}$. We attribute this to
576 two factors. First is the likely absence of aerosol features at all scales and all locations in the scan
577 area at all times. Second is the regularization used in *Typhoon* which favors a smooth motion field,
578 especially as the estimation reaches the smallest scales.

579 A transfer function describes the ratio of two spectra and, in the present work, represents the
580 attenuation of the actual wind field caused by the motion estimation as a function of wavenumber.
581 A highly idealized spectrum is constructed to serve as the reference. This is done by first locating
582 the maximum of each mean spatial spectra shown in Fig. 15. We assume that the observed power
583 at wavenumbers smaller than the peak in the spectra are accurately captured by the algorithm and
584 serve as a proper approximation of the power at those large scales. For scales smaller than the
585 peak, we extrapolate by a power-law dependence through the higher wavenumbers that mimics
586 the inertial subrange (a $\kappa^{-2/3}$ spectrum). The transfer functions are then given by the ratio of the
587 observed mean spectra over the idealized spectrum, and presented in the bottom row of Fig. 15.
588 The higher the wind speed, the more energy is missing at small scales. The ratio typically drops
589 below 50% at scales of $\approx 100 \text{ m}$ ($\kappa/2\pi \approx 0.01 \text{ m}^{-1}$) for the highest wind speeds, and $\approx 75 \text{ m}$ for
590 the lowest.

591 **6. Broader perspectives and conclusions**

592 In a recent paper, entitled *Review of turbulence measurements using ground-based wind lidars*,
593 Sathe and Mann (2013) conclude that “Non-coherent detection may also provide possible new
594 ways to estimate atmospheric turbulence, but to our knowledge it does not, so far, challenge the
595 capabilities of coherent Doppler lidars.” In this paper, we have (1) introduced a new motion
596 estimation method; (2) made the first direct comparisons of the “non-Doppler motion estimation
597 approach” with Doppler lidar; and (3) computed transfer functions to estimate the filtering effect
598 of the approach. The new motion estimation method resolves finer spatial scale flow details than
599 the traditional cross-correlation algorithm (Hamada et al. 2015). The comparisons in the time
600 domain reveal excellent correlation in terms of 10-min averages, close for example to standards
601 expected of commercial floating lidars (Carbon Trust 2013). However, the proposed approach still
602 underestimates the TKE by about 50% of what is observed by Doppler lidar. It is important to
603 keep in mind that the Doppler also provides a filtered version of the actual flow field.

604 Two horizontal components are required for wind speed and direction. The proposed approach
605 delivers dense 2-component wind fields from a single lidar, whereas a single Doppler only pro-
606 duces a single component. In addition to wind resource assessment, wind fields such as delivered
607 by *Typhoon* from REAL imagery enable the visualization and investigation of meteorological phe-
608 nomena such as vortices and fronts. They also open the possibility of studies in the Lagrangian
609 reference frame, and the tracking of flow structures or aerosol features.

610 *Acknowledgments.* This material is based upon work supported by the National Science Founda-
611 tion’s Physical and Dynamic Meteorology Program under Grant No. AGS 1228464. Dr. Christoph
612 Thomas provided helpful suggestions for data analysis.

614

Mathematical Symbols

615

- \forall for all;

616

- \subset subset of;

617

- \in in (belonging to);

618

- \mathbb{N} , \mathbb{R} the sets of natural and real numbers, respectively.

619

APPENDIX B

620

Parameters of *Typhoon*

621

Unless specified, results were obtained using the following parameters for *Typhoon*:

622

- version: cuTyphoon 1.0;

623

- wavelet basis: Daubechies, 10 vanishing moments;

624

- wavelet scales: 8 details scales considered and estimated;

625

- pyramid steps=1, scaling factor=50%;

626

- data model: DFD, smoothing kernel $\sigma = 0.5$;

627

- regularization: Horn & Schunk, $\alpha = 0.05$;

628

- data range: $[-0.5, 0.5]$, with normalization, without histogram matching.

629

References

630

Adrian, R. J., 2005: Twenty years of particle image velocimetry. *Exp. Fluids*, **39** (2), 159–169.

631 Adrian, R. J., and J. Westerweel, 2010: *Particle image velocimetry*, Vol. 30. Cambridge University
632 Press.

633 Axel, A., and J. Ailt-Wiard, 2014: Calibration certificate – HALO Photonics Stream Line 1012-55.
634 Tech. rep., Deutsche WindGuard.

635 Bailey, B. H., Ed., 2012: *Wind resource assessment: a practical guide to developing a wind*
636 *project*. John Wiley & Sons.

637 Carbon Trust, 2013: Roadmap for the commercial acceptance of floating LIDAR technology. Tech.
638 Rep. CTC819, Offshore Wind Accelerator programme, 30 pp.

639 Corpetti, T., E. Mémin, and P. Pérez, 2002: Dense estimation of fluid flows. *IEEE Trans. Pattern*
640 *Anal. Mach. Intell.*, **24** (3), 365–380.

641 Dérian, P., 2012: Wavelets and Fluid Motion Estimation. Ph.D. thesis, MATISSE,
642 Université Rennes 1, 100 pp., [Available online at http://tel.archives-ouvertes.fr/tel-00761919/PDF/theseDERIAN_v3_BU_.pdf.].

644 Dérian, P., P. Héas, C. Herzet, and E. Mémin, 2013: Wavelets and optical flow motion estimation.
645 *Num. Math. Theor. Meth. Appl.*, **6** (1), 116–137.

646 Dérian, P., P. Héas, E. Mémin, and S. Mayor, 2010: Dense motion estimation from eye-safe aerosol
647 lidar data. *International Laser Radar Conference (ILRC25)*, St Petersburg, Russia, Vol. 1, 377–
648 380, oral presentation S3O-04.

649 Dugan, J., S. Anderson, C. Piotrowski, and S. Zuckerman, 2014: Airborne infrared remote sensing
650 of riverine currents. *IEEE Trans. Geosci. Rem. Sens.*, **52** (7), 3895–3907, doi:10.1109/TGRS.
651 2013.2277815.

652 Eloranta, E., J. King, and J. Weinman, 1975: The determination of wind speeds in the boundary
653 layer by monostatic lidar. *J. Appl. Meteor.*, **14** (8), 1485–1489.

654 Fisher, N. I., 1995: *Statistical analysis of circular data*. Cambridge University Press.

655 García-Pereda, J., and R. Borde, 2014: The impact of the tracer size and the temporal gap be-
656 tween images in the extraction of atmospheric motion vectors. *J. Atmos. Ocean. Technol.*,
657 **31** (8), 1761 – 1770, URL [http://mantis.csuchico.edu/login?url=http://search.ebscohost.com/
658 login.aspx?direct=true&db=aph&AN=97381913&site=eds-live](http://mantis.csuchico.edu/login?url=http://search.ebscohost.com/login.aspx?direct=true&db=aph&AN=97381913&site=eds-live).

659 Hamada, M., 2014: Evaluations of the performance of a cross-correlation algorithm for wind
660 velocity estimation using syntetic backscatter lidar images and velocity fields. M.S. thesis,
661 Environmental Sciences, California State University, Chico, 159 pp., [Available online at
662 http://phys.csuchico.edu/lidar/publications/Masaki_Hamada_MS_thesis.pdf.].

663 Hamada, M., P. Dérian, C. F. Mauzey, and S. D. Mayor, 2015: Optimization of the cross-
664 correlation algorithm for two-component wind field estimation from single aerosol lidar data
665 and comparison with Doppler lidar. *Submitted to J. Atmos. Ocean. Technol.*

666 Held, A., T. Seith, I. M. Brooks, S. J. Norris, and S. D. Mayor, 2012: Intercomparison of lidar
667 aerosol backscatter and in-situ size distribution measurements. *European Aerosol Conference*,
668 Granada, Spain, presentation number B-WG01S2P05.

669 Horn, B. K., and B. G. Schunck, 1981: Determining optical flow. *Artif. Intell.*, **17**, 185–203.

670 Kadri Harouna, S., P. Dérian, P. Héas, and E. Mémin, 2013: Divergence-free Wavelets and High
671 Order Regularization. *Int. J. Computer Vision*, **103**, 80–99, URL [http://hal.archives-ouvertes.fr/
672 hal-00646104](http://hal.archives-ouvertes.fr/hal-00646104).

- 673 Kaimal, J. C., and J. J. Finnigan, 1994: *Atmospheric Boundary Layer Flows*. Oxford University
674 Press, 200 Madison Ave., New York, NY 10016, 289 pp.
- 675 Kanak, K. M., 2005: Numerical simulation of dust devil-scale vortices. *Quart. J. Roy. Meteor.*
676 *Soc.*, **131 (607)**, 1271–1292.
- 677 Leese, J., C. Novack, and B. Clark, 1971: An automated technique for obtained cloud motion from
678 geosynchronous satellite data using cross correlation. *J. Appl. Meteor.*, **10**, 118–132.
- 679 Mallat, S., 2008: *A Wavelet Tour of Signal Processing: The Sparse Way*. Academic Press.
- 680 Mann, J., A. Pena, F. Bingol, R. Wagner, and M. S. Courtney, 2010: Lidar scanning of momentum
681 flux in and above the atmospheric surface layer. *J. Atmos. Ocean. Technol.*, **27**, 959–976.
- 682 Mann, J., and Coauthors, 2009: Comparison of 3D turbulence measurements using three staring
683 wind lidars and a sonic anemometer. *Meteor. Z.*, **18**, 135–140.
- 684 Mauzey, C. F., P. Dérian, and S. D. Mayor, 2014: Wavelet-based optical flow for real-time wind
685 estimation using CUDA. *GPU Technology Conference*, San Diego, CA, poster P4253.
- 686 Mauzey, C. F., J. P. Lowe, and S. D. Mayor, 2012: Real-time wind velocity estimation from aerosol
687 lidar data using graphics hardware. *GPU Technology Conference*, San Diego, CA, poster AV10.
- 688 Mayor, S. D., and E. W. Eloranta, 2001: Two-dimensional vector wind fields from volume imaging
689 lidar data. *J. Appl. Meteor.*, **40 (8)**, 1331–1346.
- 690 Mayor, S. D., J. P. Lowe, and C. F. Mauzey, 2012: Two-component horizontal aerosol motion
691 vectors in the atmospheric surface layer from a cross-correlation algorithm applied to scanning
692 elastic backscatter lidar data. *J. Atmos. Ocean. Technol.*, **29 (11)**, 1585–1602.

- 693 Mayor, S. D., and S. M. Spuler, 2004: Raman-shifted eye-safe aerosol lidar. *Appl. Optics*, **43** (19),
694 3915–3924.
- 695 Mayor, S. D., S. M. Spuler, B. M. Morley, and E. Loew, 2007: Polarization lidar at 1.54 μm and
696 observations of plumes from aerosol generators. *Opt. Eng.*, **46** (9), 096 201–096 201.
- 697 Melville, W. K., and P. Matusov, 2002: Distribution of breaking waves at the ocean surface. *Nature*,
698 **417** (6884), 58–63.
- 699 Päschke, E., R. Leinweber, and V. Lehmann, 2014: A one year comparison of 482 mhz radar wind
700 profiler, rs92-sgp radiosonde and 1.5 μm Doppler lidar wind measurements. *Atmos. Meas. Tech.*
701 *Discuss.*, **7** (11), 11 439–11 479.
- 702 Patton, E. G., and Coauthors, 2011: The canopy horizontal array turbulence study. *Bull. Amer.*
703 *Meteor. Soc.*, **92** (5), 593–611.
- 704 Pearson, G., F. Davies, and C. Collier, 2009: An analysis of the performance of the UFAM pulsed
705 Doppler lidar for observing the boundary layer. *J. Atmos. Ocean. Technol.*, **26**, 240–250.
- 706 Sasano, Y., H. Hirohara, T. Yamasaki, H. Shimizu, N. Takeuchi, and T. Kawamura, 1982: Horizontal
707 wind vector determination from the displacement of aerosol distribution patterns observed
708 by a scanning lidar. *J. Appl. Meteor.*, **21** (10), 1516–1523.
- 709 Sathe, A., and J. Mann, 2012: Measurement of turbulence spectra using scanning pulsed wind
710 lidars. *J. Geophys. Res.*, **117** (D1), doi:10.1029/2011JD016786.
- 711 Sathe, A., and J. Mann, 2013: A review of turbulence measurements using ground-based wind
712 lidars. *Atmos. Meas. Tech. Discuss.*, **6** (4), 6815–6871.
- 713 Sathe, A., J. Mann, J. Gottschall, and M. S. Courtney, 2011: Can wind lidars measure turbulence?
714 *J. Atmos. Ocean. Technol.*, **28**, 853–868.

715 Scambos, T. A., M. J. Dutkiewicz, J. C. Wilson, and R. A. Bindschadler, 1992: Application of im-
716 age cross-correlation to the measurement of glacier velocity using satellite image data. *Remote*
717 *Sens. Environ.*, **42** (3), 177–186.

718 Schmetz, J., K. Holmund, J. Hoffman, B. Strauss, B. Mason, V. Gaertner, A. Koch, and L. V. D.
719 Berg, 1993: Operational cloud-motion winds from Meteosat infrared images. *J. Appl. Meteor.*,
720 **32** (7), 1206–1225.

721 Schmidt, H., and U. Schumann, 1989: Coherent structure of the convective boundary layer derived
722 from large-eddy simulations. *J. Fluid Mech.*, **200**, 511–562.

723 Schols, J., and E. Eloranta, 1992: Calculation of area-averaged vertical profiles of the horizontal
724 wind velocity from volume-imaging lidar data. *J. Geophys. Res.*, **97** (D17), 18 395–18 407.

725 Spuler, S. M., and S. D. Mayor, 2005: Scanning eye-safe elastic backscatter lidar at 1.54 μ m. *J.*
726 *Atmos. Ocean. Technol.*, **22** (6), 696–703.

727 Stawiarski, C., K. Träumner, C. Knigge, and R. Calhoun, 2013: Scopes and challenges of dual-
728 Doppler lidar wind measurements—an error analysis. *J. Atmos. Ocean. Technol.*, **30** (9), 2044–
729 2062.

730 Stumpf, A., J. Malet, P. Allemand, G. Skupinski, and M. Pierrot-Deseilligny, 2013: Terrestrial
731 multi-view photogrammetry for landslide monitoring. *AGU Fall Meeting Abstracts*, A5.

732 Sullivan, P. P., and E. G. Patton, 2011: The effect of mesh resolution on convective boundary layer
733 statistics and structures generated by large-eddy simulation. *J. Atmos. Sci.*, **68** (10), 2395–2415.

734 Van Dyke, M., 1982: *An album of fluid motion*. Parabolic Press Stanford, CA.

735 Weber, B., D. Wuertz, D. Welsh, and R. McPeck, 1993: Quality controls for profiler measurements
736 of winds and rass temperatures. *J. Atmos. Ocean. Technol.*, **10** (4), 452–464.

737 **LIST OF TABLES**

738 **Table 1.** Main parameters of DL and REAL measurements for the temporal and spatial
739 validation experiments. 38

740 **Table 2.** RMS error, linear regression variables (slope, offset), correlation coefficient
741 R^2 , number of points and recovery percentage w.r.t. DL reference for the 10-
742 min averaged wind component u (west-east), for the temporal validation results
743 (Sec. 5.a). 39

744 **Table 3.** RMS error, linear regression variables (slope, offset), correlation coefficient R^2 ,
745 number of points and recovery percentage w.r.t. DL reference for the 10-min
746 averaged wind component v (south-north), for the temporal validation results
747 (Sec. 5.a). 40

TABLE 1. Main parameters of DL and REAL measurements for the temporal and spatial validation experiments.

	Temporal validation		Spatial validation	
	Doppler	REAL	Doppler	REAL
scan type	VAD	PPI	STARE	PPI
azimuth (°)	–	[–15;45]	45	[15;75]
elevation (°)	–	4	2	2
range (km)	–	[0.5;5.5]	[0;5]	[0.5;5.5]
components	2	2	1	2
δx (m)	–	8	48	8
δt (s)	15 ± 1	17	1	17

748 TABLE 2. RMS error, linear regression variables (slope, offset), correlation coefficient R^2 , number of points
 749 and recovery percentage w.r.t. DL reference for the 10-min averaged wind component u (west-east), for the
 750 temporal validation results (Sec. 5.a).

case	RMSE (m s^{-1})	slope	offset (m s^{-1})	R^2	# points	% recovery
light	0.17	1.047	-0.01	0.951	61	84.7
moderate	0.29	0.974	-0.05	0.979	72	100
strong	0.33	0.938	0.32	0.984	72	100
15 days	0.29	0.989	-0.03	0.995	892	99.1

751 TABLE 3. RMS error, linear regression variables (slope, offset), correlation coefficient R^2 , number of points
 752 and recovery percentage w.r.t. DL reference for the 10-min averaged wind component v (south-north), for the
 753 temporal validation results (Sec. 5.a).

case	RMSE (m s^{-1})	slope	offset (m s^{-1})	R^2	# points	% recovery
light	0.27	0.660	-0.02	0.600	61	84.7
moderate	0.23	0.999	0.00	0.991	72	100
strong	0.34	0.897	-0.72	0.929	72	100
15 days	0.29	1.001	0.03	0.997	892	99.1

754 **LIST OF FIGURES**

755 **Fig. 1.** Example of preprocessing applied to a horizontal scan collected on 3 October 2013 at
756 23:14:10 UTC. Panel (a) is the preprocessed backscatter data. Panel (b) is the raw SNR
757 (7), revealing a $1/r^2$ decay. Panel (c) is the image SNR (8) computed using a 384 m win-
758 dows. Panel (d) is the valid data domain computed from image SNR. Motion is estimated in
759 the white area only, excluding far-range noisy regions. The far-range boundary (9) of this
760 area is also shown in (a) as a white line. Resulting, decimated vector flow field has been
761 added to the valid area in (d). 43

762 **Fig. 2.** Illustration of the experimental design for the temporal validation of motion estimation vec-
763 tors. Panel (a) is a short sequence of 3 consecutive PPI scans collected on 14 October 2013
764 by the REAL. The displayed area is a close-up centered on the Doppler lidar (white marker)
765 used for validation. The copper shading indicates the intensity, in dB, of aerosol backscatter.
766 A large aerosol feature is being advected south-east and passes over the DL. Panel (b), and
767 (c) show the velocity fields estimated by *Typhoon* (black arrows) from each pair of scans;
768 they were decimated by a factor of 6 along both dimensions for the sake of visualization.
769 Measurements from the DL (red arrows) at 100 m AGL show a good agreement with esti-
770 mates, with a wind speed of $\approx 5.4 \text{ m s}^{-1}$ 44

771 **Fig. 3.** Distribution of days in terms of valid image SNR (Sec. 4.b) in a 50 m radius around DL loca-
772 tion (horizontal axis) versus mean wind speed measured by the DL at 100 m AGL (vertical
773 axis), during daytime. Days for which time-series are presented (Fig. 6, 7, 8) are repre-
774 sented with a black diamond. A total of 57 days are considered, of which 9 have less than
775 60% valid SNR_{img} and are not visible here. The 15 days having more than 85% valid SNR_{img}
776 were investigated for the statistics shown in Fig. 9. 45

777 **Fig. 4.** Wind field obtained by *Typhoon* 3 October 2013 at 18:45:07 UTC, superimposed on the first
778 scan of the pair used for estimation. Wind velocity was $\approx 14 \text{ m s}^{-1}$. The motion field was
779 decimated along both dimensions by a factor of 24. The turquoise circle represents the cone
780 section sampled by the DL during the VAD scan. 46

781 **Fig. 5.** Wind field obtained by *Typhoon* 23 October 2013 at 23:32:04 UTC, superimposed on the
782 first scan of the pair used for estimation. The upper panel shows a close up on a vortex of
783 radius $\approx 200 \text{ m}$. The motion field was decimated along both dimensions by a factor of 6
784 and 12 for the top and bottom panels, respectively. The turquoise circle represents the cone
785 section sampled by the DL during the VAD scan. 47

786 **Fig. 6.** Times series of wind speed (top) and direction (bottom) as measured by the DL (blue) and
787 estimated by proposed method (orange), for a 12-hour period starting 23 October 2013 at
788 15:00 UTC (light wind case). Light + markers are instantaneous values, darker lines are
789 the 10-min rolling averages. The rapid change in direction is the signature of the vortex
790 presented in Fig. 5. 48

791 **Fig. 7.** Times series of wind speed (top) and direction (bottom) as measured by the DL (blue) and
792 estimated by proposed method (orange), for a 12-hour period starting 17 September 2013
793 at 15:00 UTC (moderate wind case). Light + markers are instantaneous values, darker lines
794 are the 10-min rolling averages. 49

795 **Fig. 8.** Times series of wind speed (top) and direction (bottom) as measured by the DL (blue) and
796 estimated by proposed method (orange), for a 12-hour period starting 9 October 2013 at
797 15:00 UTC (strong wind case). Light + markers are instantaneous values, darker lines are
798 the 10-min rolling averages. 50

799 **Fig. 9.** Panels (a) and (b) are scatter plots of 10-min averaged wind components u and v measured
800 by the DL at 100 m AGL (horizontal axis) versus estimated by *Typhoon* (vertical axis),
801 combining the 15 days having $> 85\%$ valid SNR_{img} during daytime (Fig. 3) – 892 points
802 total. Panels (c) and (d) are the distribution of differences for the same dataset. 51

803 **Fig. 10.** Scatter plot of the TKE measured over 10-min intervals, by the DL at 100 m AGL (horizontal
804 axis) versus estimated by the proposed method (vertical axis) – 892 points total. The gray
805 shading indicated the mean wind speed measured over the interval. A linear regression
806 (dashed line) gives a slope of 0.49 and offset of -0.03. 52

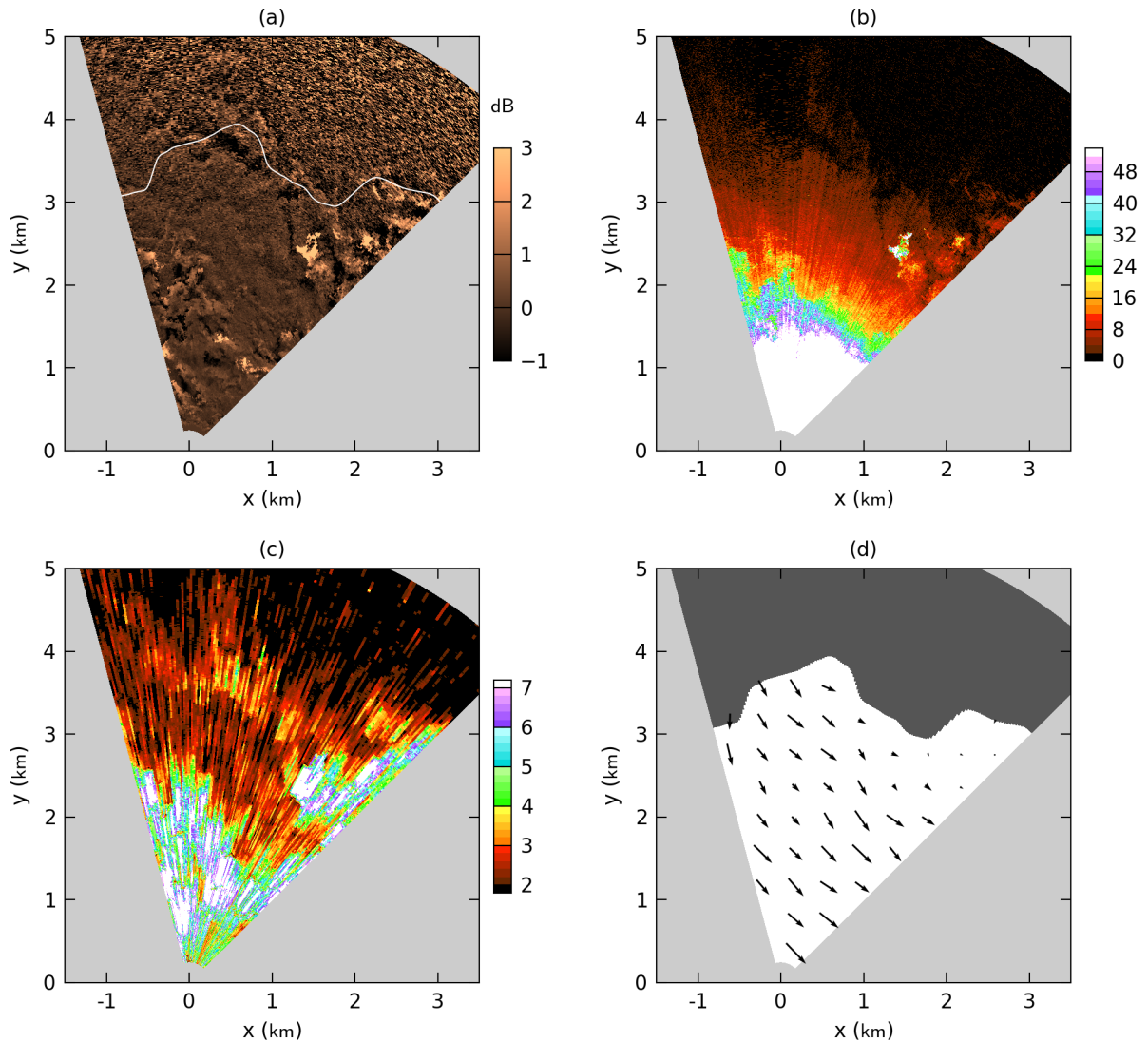
807 **Fig. 11.** Illustration of the experimental design for the spatial validation of motion estimation vectors.
808 Panel (a) shows subsets of 2 consecutive PPI scans collected on 8 January 2014 by the
809 REAL. The displayed area is a close-up centered on the DL line-of-sight at 45° azimuth
810 (dashed white line). The copper shading indicates the intensity, in dB, of aerosol backscatter.
811 A large aerosol feature is being advected north. Panel (b) shows the velocity field (black
812 arrows) estimated by *Typhoon* from these two scans; the vector field was decimated by
813 a factor of 15 along both dimensions for the sake of visualization. The color shading in
814 the background indicates the corresponding radial velocity. Panel (c) compares the radial
815 velocities measured by the Doppler (black line) and extracted from the 2-component field
816 estimated by *Typhoon* (red line), along the DL line-of-sight. 53

817 **Fig. 12.** Comparison of *radial wind component* at 45° azimuth and 2° elevation measured by the DL
818 (top) and estimated by proposed method (bottom), as a function of time (horizontal axis)
819 and range (vertical axis), for a 8-hour period starting 8 January 2014 at 17:00 UTC. Gray
820 shading indicates missing or discarded data. 54

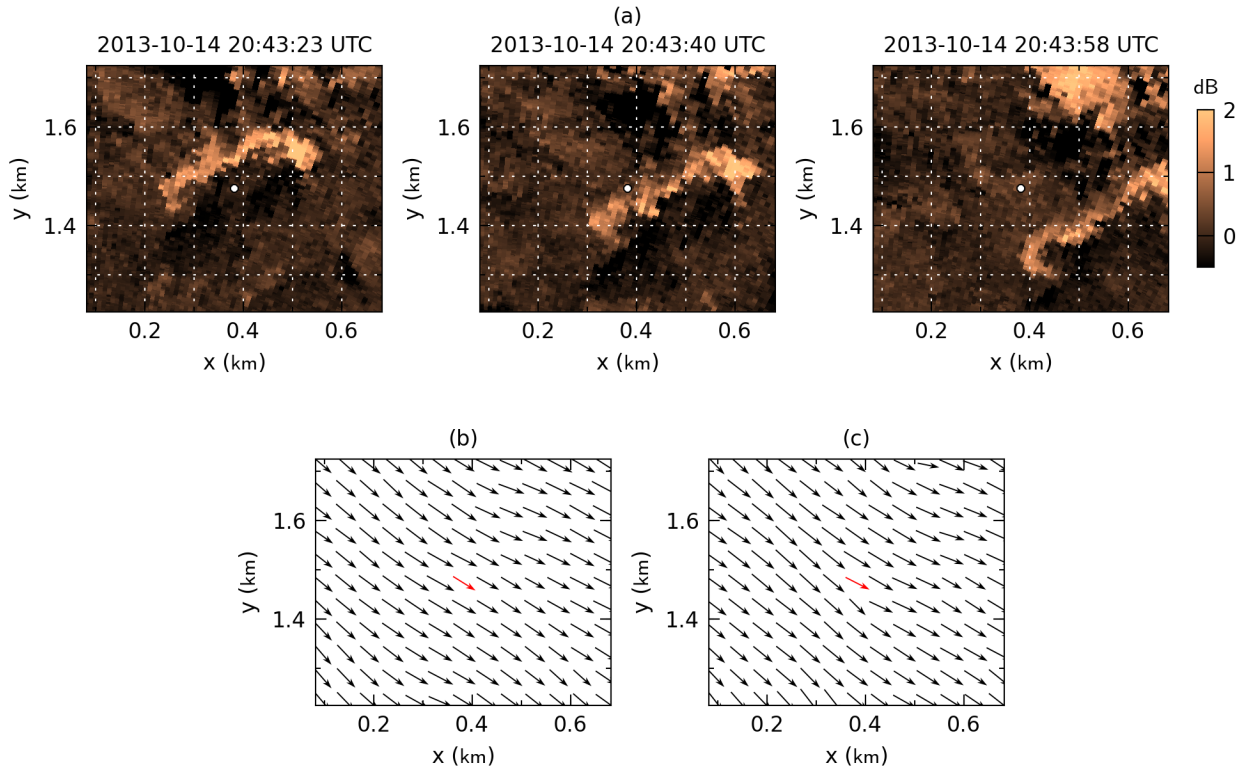
821 **Fig. 13.** Panel (a), scatter plot of 10-min averaged radial wind component measured by the DL (hor-
822 izontal axis) versus estimated by the proposed method (vertical axis). Color indicates the
823 range, from blue (0.5 km) to red (3 km). Panel (b), histogram of differences. Panel (c), slope
824 of linear regression as a function of range. Panel (d), R^2 coefficient as a function of range.
825 Dashed red lines indicate overall slope and R^2 values. 55

826 **Fig. 14.** Temporal spectra for stream-wise component u_s (left) and cross-stream component v_n (right)
827 obtained by *Typhoon* (solid lines) and the DL (dashed lines). The shadings from light to
828 dark gray correspond to wind speed ranges of [0;4], [4;8], and [8;12] m s^{-1} . The dotted line
829 represents the $-2/3$ slope of the inertial subrange predicted by theory. 56

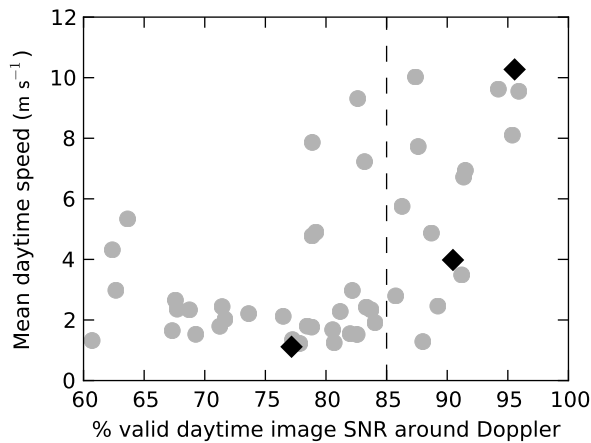
830 **Fig. 15.** Slices of 2D power spectral density (top) and corresponding transfer functions (bottom), for
831 stream-wise component u in the streamwise (a) and cross-stream (b) directions, and cross-
832 wise component v in the streamwise (c) and cross-stream (d) directions. The shadings from
833 light gray to black correspond to wind speed ranges of [0;4], [4;8], [8;12] and [12;16] m s^{-1} .
834 The dotted line represents the $-2/3$ slope of the inertial subrange predicted by theory. 57



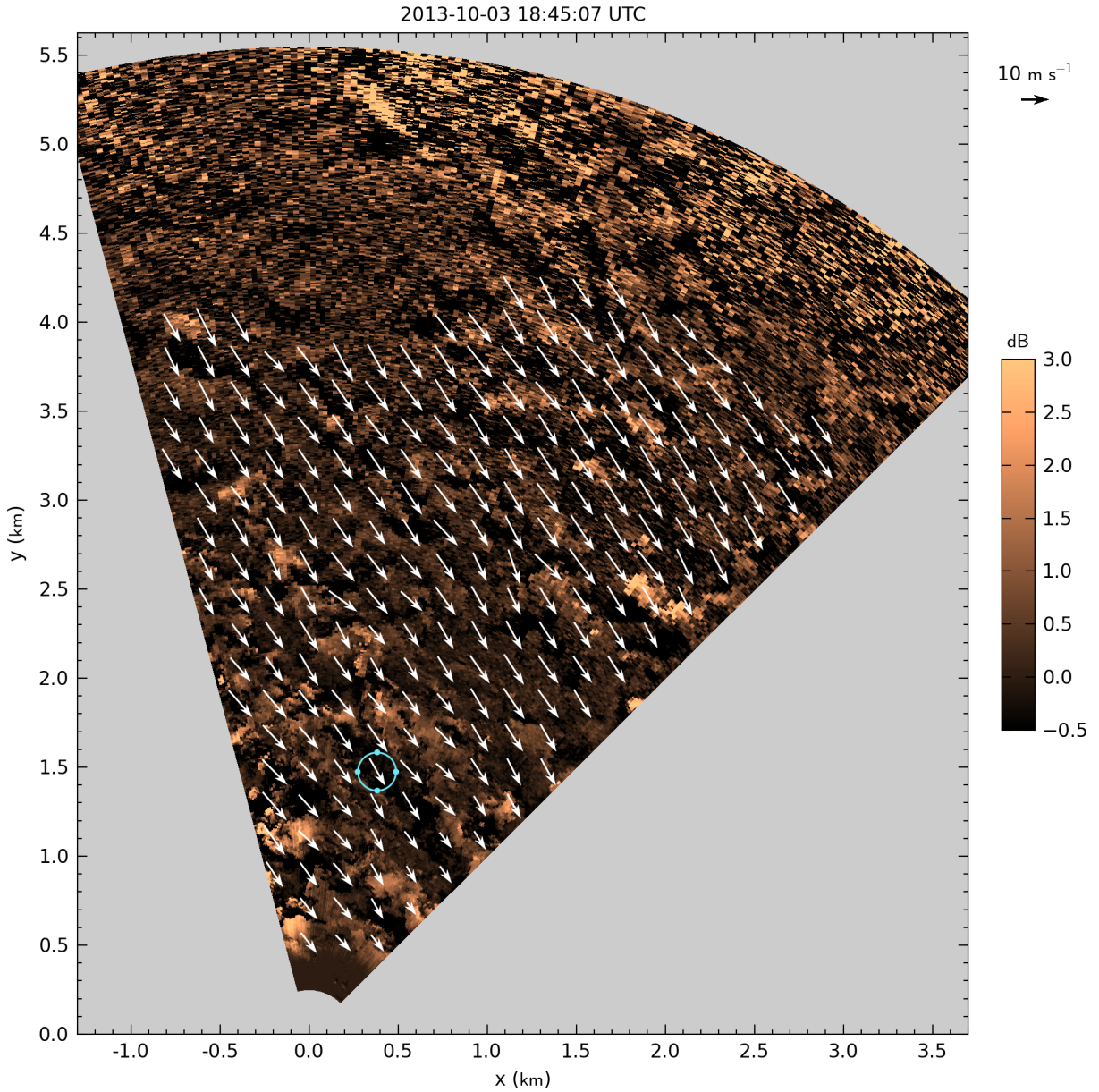
835 FIG. 1. Example of preprocessing applied to a horizontal scan collected on 3 October 2013 at 23:14:10 UTC.
 836 Panel (a) is the preprocessed backscatter data. Panel (b) is the raw SNR (7), revealing a $1/r^2$ decay. Panel (c) is
 837 the image SNR (8) computed using a 384 m window. Panel (d) is the valid data domain computed from image
 838 SNR. Motion is estimated in the white area only, excluding far-range noisy regions. The far-range boundary (9)
 839 of this area is also shown in (a) as a white line. Resulting, decimated vector flow field has been added to the
 840 valid area in (d).



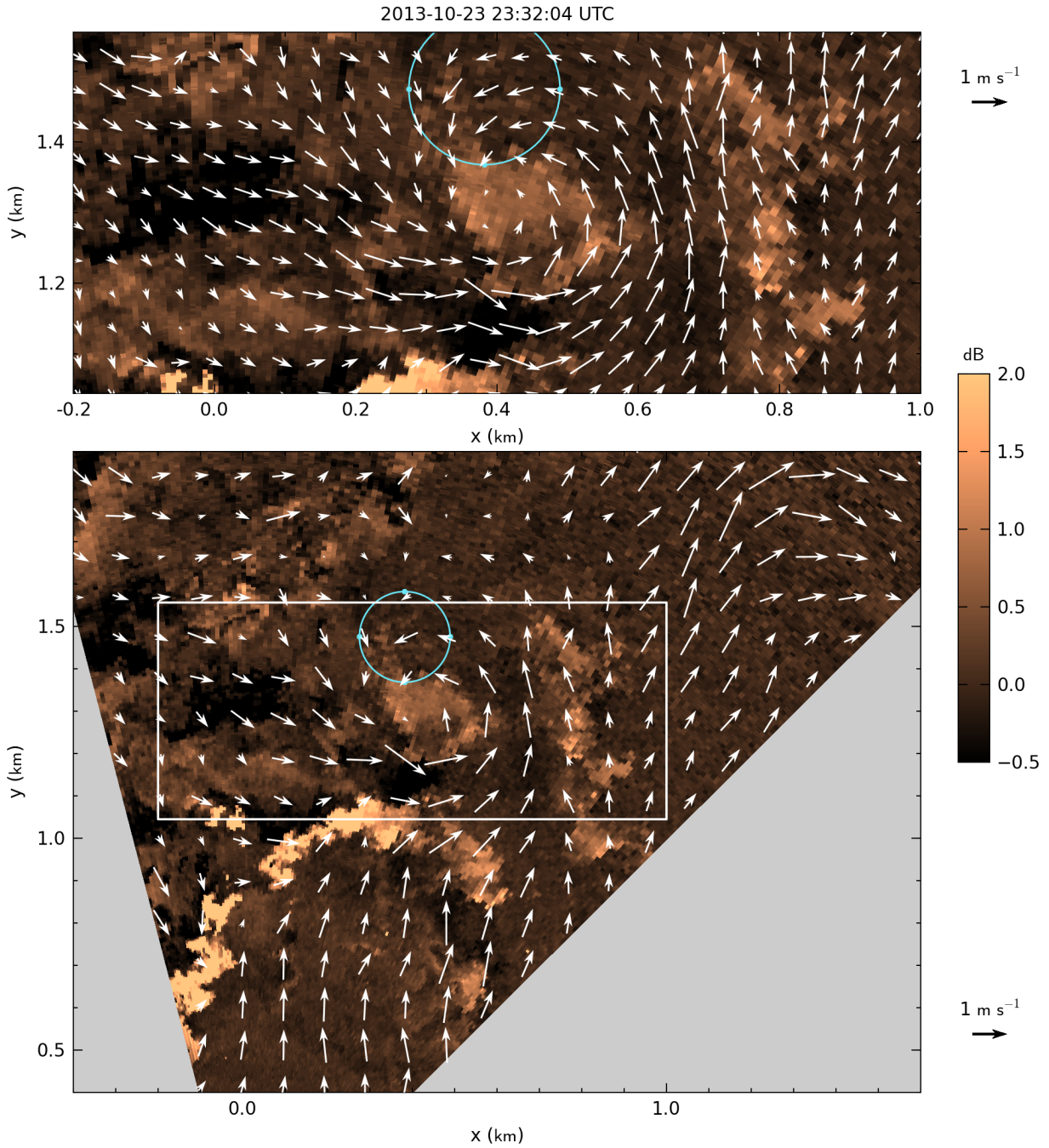
841 FIG. 2. Illustration of the experimental design for the temporal validation of motion estimation vectors. Panel
 842 (a) is a short sequence of 3 consecutive PPI scans collected on 14 October 2013 by the REAL. The displayed
 843 area is a close-up centered on the Doppler lidar (white marker) used for validation. The copper shading indicates
 844 the intensity, in dB, of aerosol backscatter. A large aerosol feature is being advected south-east and passes over
 845 the DL. Panel (b), and (c) show the velocity fields estimated by *Typhoon* (black arrows) from each pair of scans;
 846 they were decimated by a factor of 6 along both dimensions for the sake of visualization. Measurements from
 847 the DL (red arrows) at 100 m AGL show a good agreement with estimates, with a wind speed of $\approx 5.4 \text{ m s}^{-1}$.



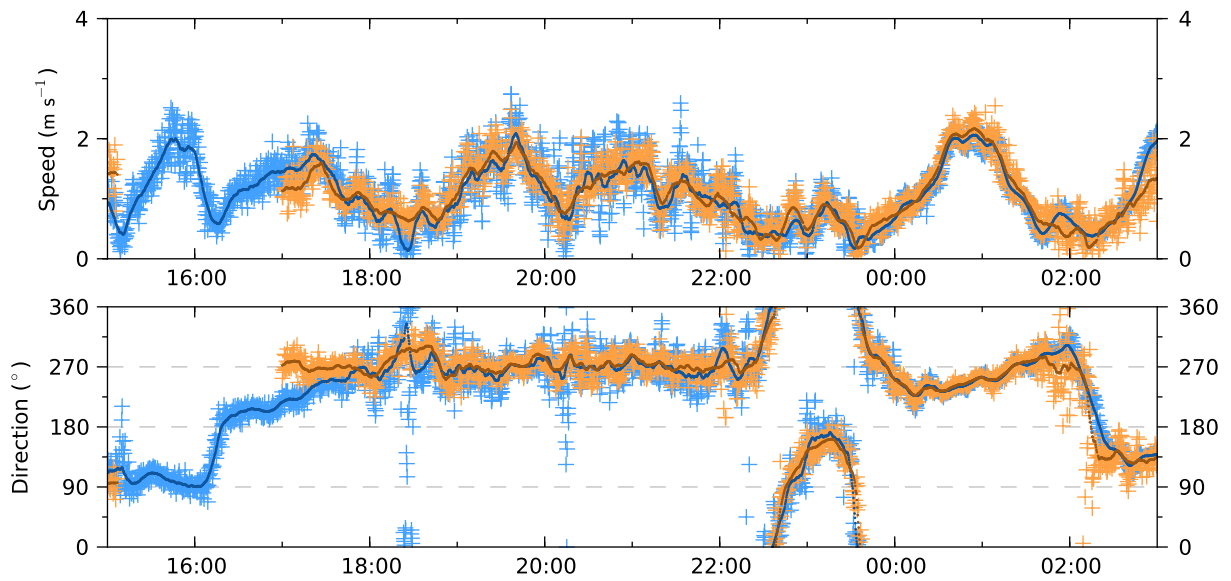
848 FIG. 3. Distribution of days in terms of valid image SNR (Sec. 4.b) in a 50 m radius around DL location
 849 (horizontal axis) versus mean wind speed measured by the DL at 100 m AGL (vertical axis), during daytime.
 850 Days for which time-series are presented (Fig. 6, 7, 8) are represented with a black diamond. A total of 57 days
 851 are considered, of which 9 have less than 60% valid SNR_{img} and are not visible here. The 15 days having more
 852 than 85% valid SNR_{img} were investigated for the statistics shown in Fig. 9.



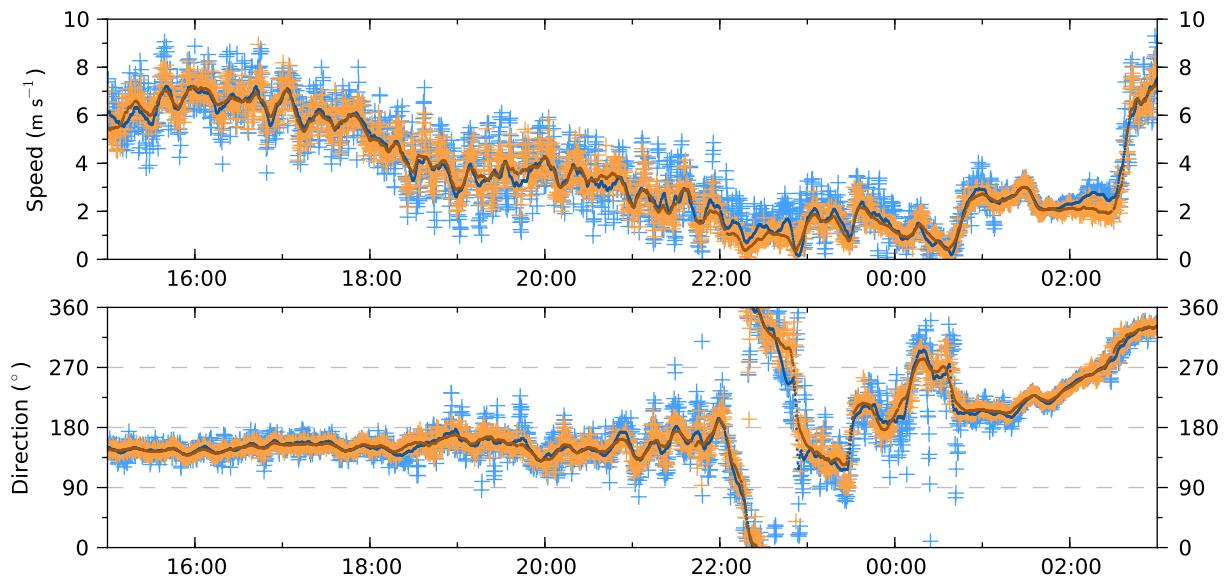
853 FIG. 4. Wind field obtained by *Typhoon* 3 October 2013 at 18:45:07 UTC, superimposed on the first scan
 854 of the pair used for estimation. Wind velocity was $\approx 14 \text{ m s}^{-1}$. The motion field was decimated along both
 855 dimensions by a factor of 24. The turquoise circle represents the cone section sampled by the DL during the
 856 VAD scan.



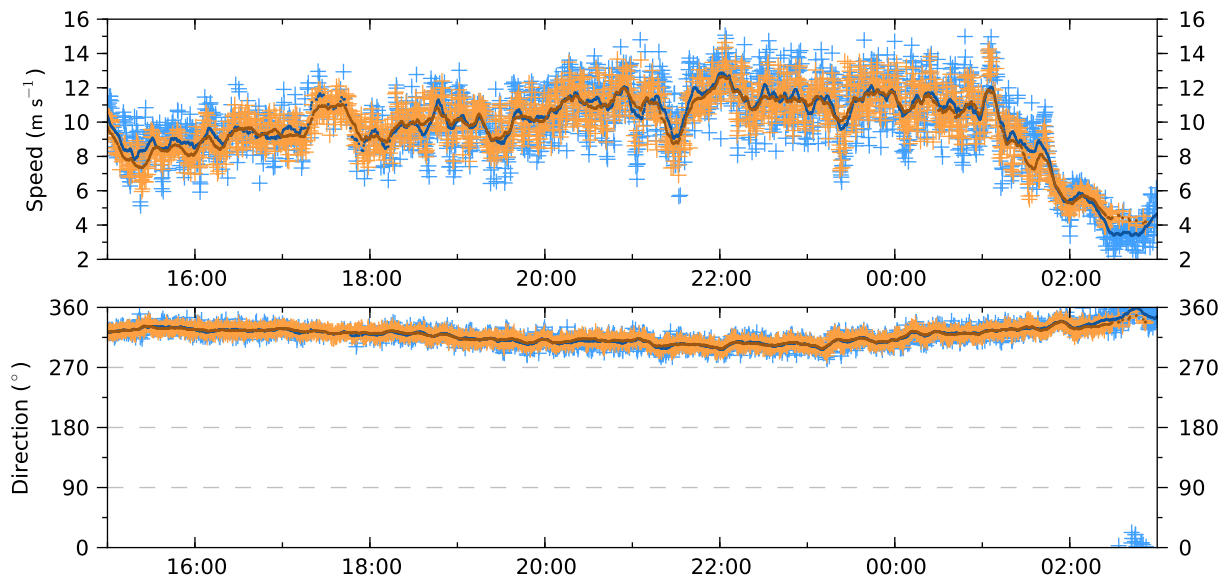
857 FIG. 5. Wind field obtained by *Typhoon* 23 October 2013 at 23:32:04 UTC, superimposed on the first scan of
 858 the pair used for estimation. The upper panel shows a close up on a vortex of radius ≈ 200 m. The motion field
 859 was decimated along both dimensions by a factor of 6 and 12 for the top and bottom panels, respectively. The
 860 turquoise circle represents the cone section sampled by the DL during the VAD scan.



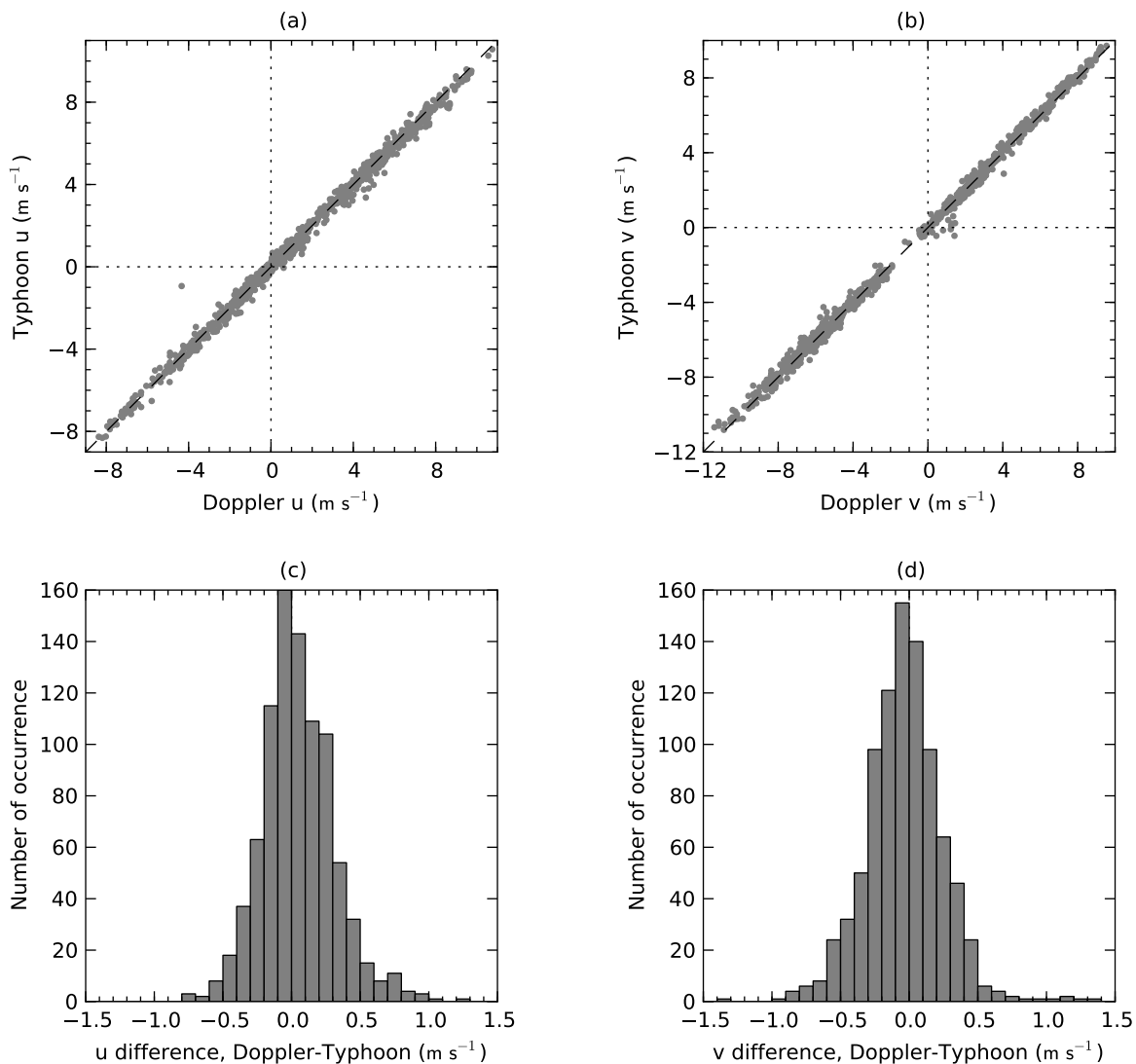
861 FIG. 6. Times series of wind speed (top) and direction (bottom) as measured by the DL (blue) and estimated
 862 by proposed method (orange), for a 12-hour period starting 23 October 2013 at 15:00 UTC (light wind case).
 863 Light + markers are instantaneous values, darker lines are the 10-min rolling averages. The rapid change in
 864 direction is the signature of the vortex presented in Fig. 5.



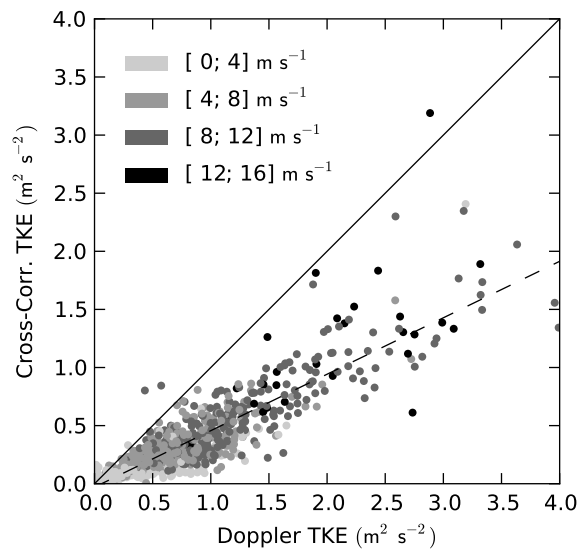
865 FIG. 7. Times series of wind speed (top) and direction (bottom) as measured by the DL (blue) and estimated
 866 by proposed method (orange), for a 12-hour period starting 17 September 2013 at 15:00 UTC (moderate wind
 867 case). Light + markers are instantaneous values, darker lines are the 10-min rolling averages.



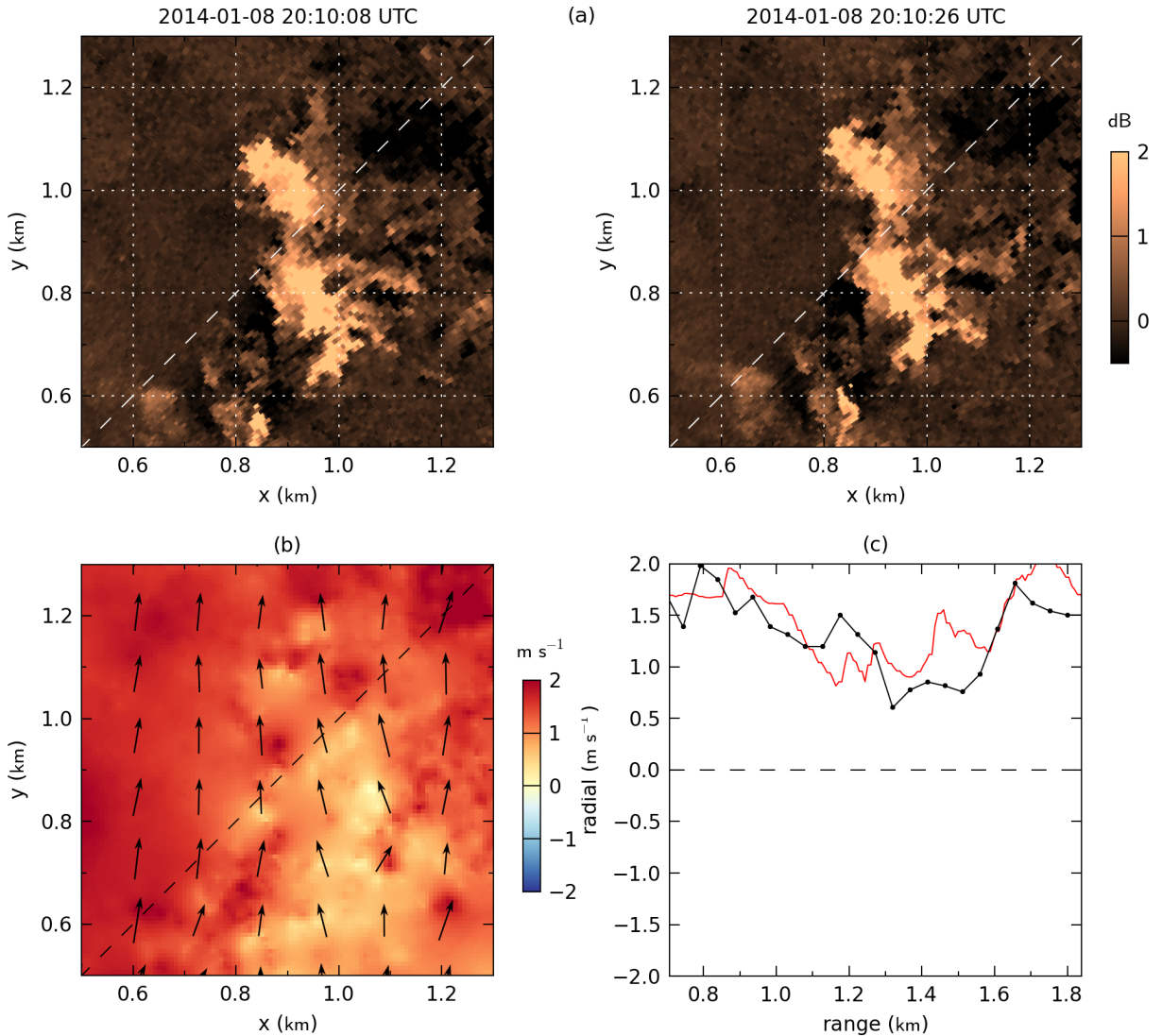
868 FIG. 8. Times series of wind speed (top) and direction (bottom) as measured by the DL (blue) and estimated
 869 by proposed method (orange), for a 12-hour period starting 9 October 2013 at 15:00 UTC (strong wind case).
 870 Light + markers are instantaneous values, darker lines are the 10-min rolling averages.



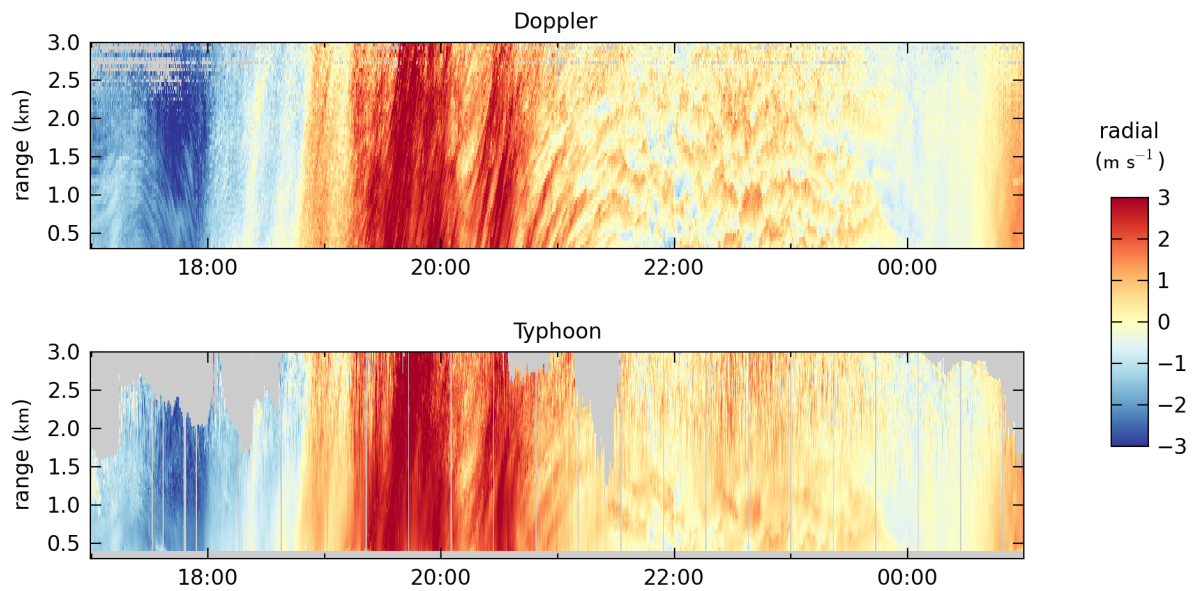
871 FIG. 9. Panels (a) and (b) are scatter plots of 10-min averaged wind components u and v measured by the DL at
 872 100 m AGL (horizontal axis) versus estimated by *Typhoon* (vertical axis), combining the 15 days having $> 85\%$
 873 valid SNR_{img} during daytime (Fig. 3) – 892 points total. Panels (c) and (d) are the distribution of differences for
 874 the same dataset.



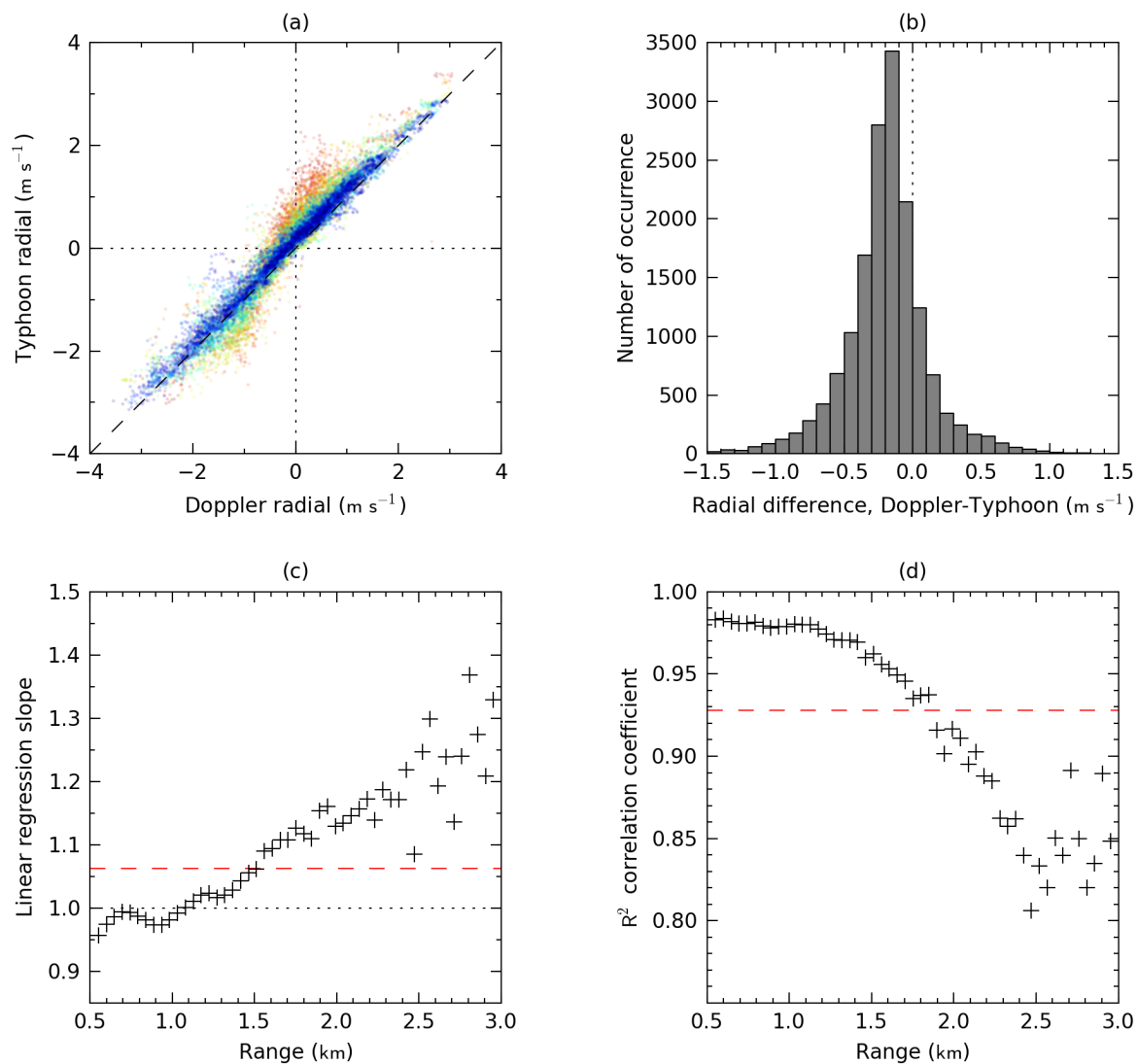
875 FIG. 10. Scatter plot of the TKE measured over 10-min intervals, by the DL at 100 m AGL (horizontal axis)
 876 versus estimated by the proposed method (vertical axis) – 892 points total. The gray shading indicated the mean
 877 wind speed measured over the interval. A linear regression (dashed line) gives a slope of 0.49 and offset of -0.03.



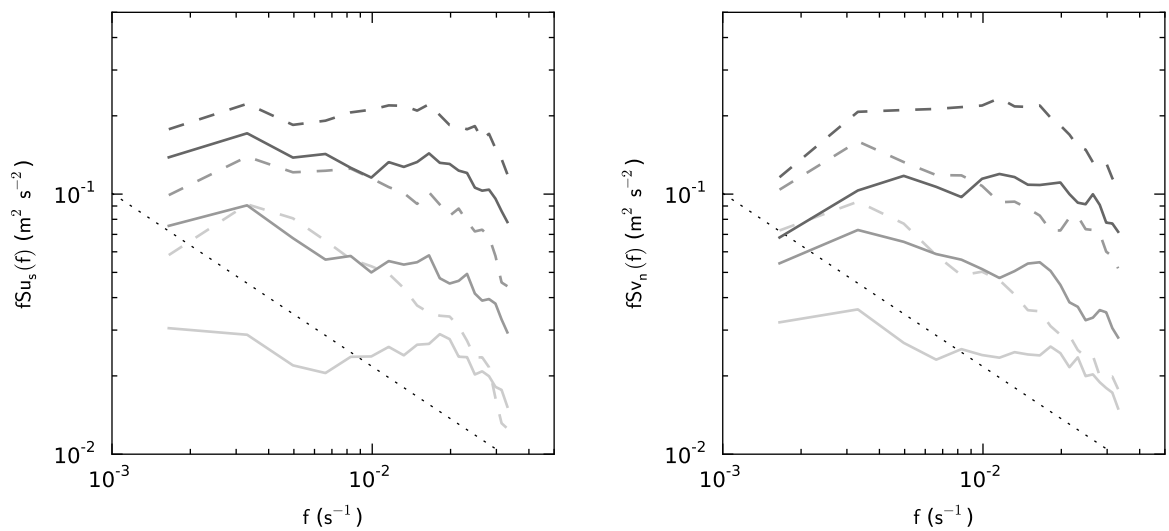
878 FIG. 11. Illustration of the experimental design for the spatial validation of motion estimation vectors. Panel
 879 (a) shows subsets of 2 consecutive PPI scans collected on 8 January 2014 by the REAL. The displayed area is
 880 a close-up centered on the DL line-of-sight at 45° azimuth (dashed white line). The copper shading indicates
 881 the intensity, in dB, of aerosol backscatter. A large aerosol feature is being advected north. Panel (b) shows the
 882 velocity field (black arrows) estimated by *Typhoon* from these two scans; the vector field was decimated by a
 883 factor of 15 along both dimensions for the sake of visualization. The color shading in the background indicates
 884 the corresponding radial velocity. Panel (c) compares the radial velocities measured by the Doppler (black line)
 885 and extracted from the 2-component field estimated by *Typhoon* (red line), along the DL line-of-sight.



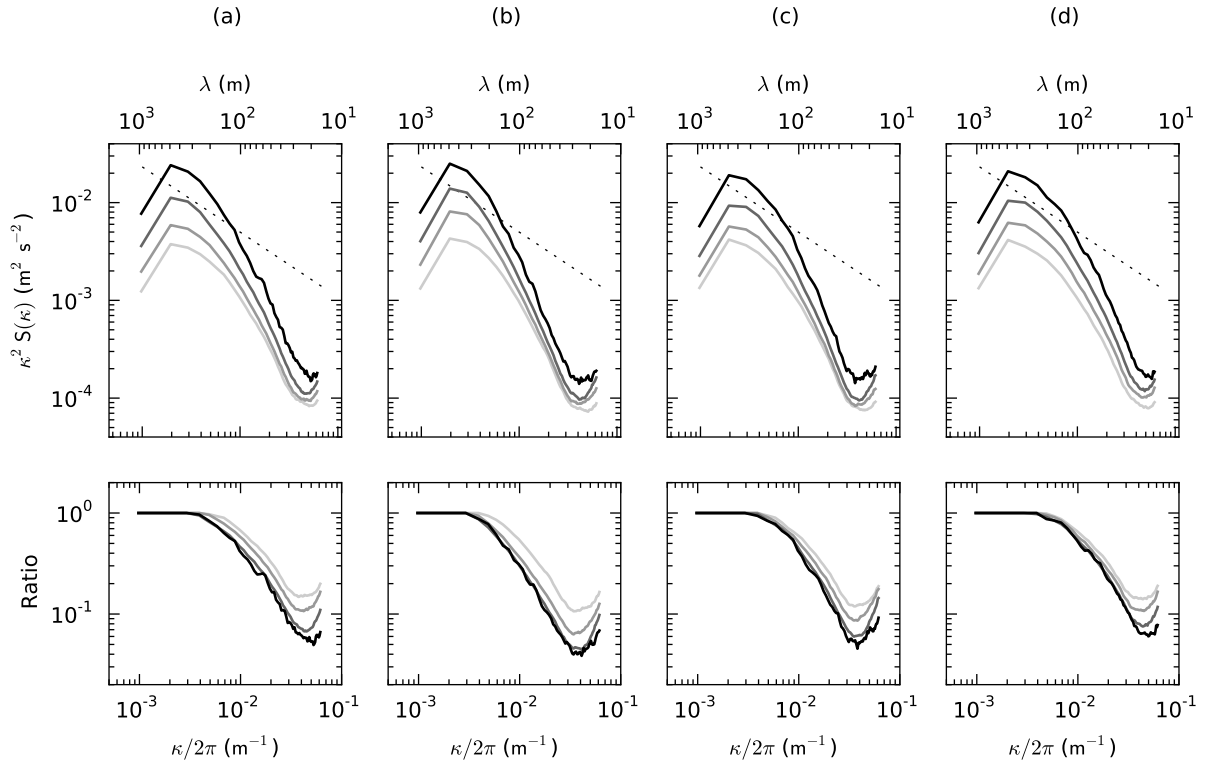
886 FIG. 12. Comparison of *radial wind component* at 45° azimuth and 2° elevation measured by the DL (top)
 887 and estimated by proposed method (bottom), as a function of time (horizontal axis) and range (vertical axis), for
 888 a 8-hour period starting 8 January 2014 at 17:00 UTC. Gray shading indicates missing or discarded data.



889 FIG. 13. Panel (a), scatter plot of 10-min averaged radial wind component measured by the DL (horizontal
 890 axis) versus estimated by the proposed method (vertical axis). Color indicates the range, from blue (0.5 km) to
 891 red (3 km). Panel (b), histogram of differences. Panel (c), slope of linear regression as a function of range. Panel
 892 (d), R^2 coefficient as a function of range. Dashed red lines indicate overall slope and R^2 values.



893 FIG. 14. Temporal spectra for stream-wise component u_s (left) and cross-stream component v_n (right) obtained
 894 by *Typhoon* (solid lines) and the DL (dashed lines). The shadings from light to dark gray correspond to wind
 895 speed ranges of [0;4], [4;8], and [8;12] m s⁻¹. The dotted line represents the -2/3 slope of the inertial subrange
 896 predicted by theory.



897 FIG. 15. Slices of 2D power spectral density (top) and corresponding transfer functions (bottom), for stream-
 898 wise component u in the streamwise (a) and cross-stream (b) directions, and cross-wise component v in the
 899 streamwise (c) and cross-stream (d) directions. The shadings from light gray to black correspond to wind speed
 900 ranges of $[0;4]$, $[4;8]$, $[8;12]$ and $[12;16]$ m s^{-1} . The dotted line represents the $-2/3$ slope of the inertial subrange
 901 predicted by theory.